

# DiffeoMorph: Learning to Morph 3D Shapes Using Differentiable Agent-Based Simulations

Seong Ho Pahng,<sup>1, 2, 3</sup> Guoye Guan,<sup>2, 3</sup> Benjamin Fefferman,<sup>3, 4, 5</sup> and Sahand Hormoz<sup>2, 3, 5, \*</sup>

<sup>1</sup>*Department of Chemistry and Chemical Biology, Harvard University, Massachusetts 02138, USA*

<sup>2</sup>*Department of Systems Biology, Harvard Medical School, Boston, Massachusetts 02115, USA*

<sup>3</sup>*Department of Data Science, Dana-Farber Cancer Institute, Boston, Massachusetts 02215, USA*

<sup>4</sup>*Departments of Biomedical Informatics, Harvard Medical School, Boston, Massachusetts 02215, USA*

<sup>5</sup>*Broad Institute of MIT and Harvard, Cambridge, Massachusetts 02142, USA*

(Dated: December 22, 2025)

Biological systems can form complex three-dimensional structures through the collective behavior of identical agents—cells that follow the same internal rules and communicate without central control. How such distributed control gives rise to precise global patterns remains a central question not only in developmental biology but also in distributed robotics, programmable matter, and multi-agent learning. Here, we introduce DiffeoMorph, an end-to-end differentiable framework for learning a morphogenesis protocol that guides a population of agents to morph into a target 3D shape. Each agent updates its position and internal state using an attention-based  $SE(3)$ -equivariant graph neural network, based on its own internal state and signals received from other agents. To train this system, we introduce a new shape-matching loss based on the 3D Zernike polynomials, which compares the predicted and target shapes as continuous spatial distributions, not as discrete point clouds, and is invariant to agent ordering, number of agents, and rigid-body transformations. To enforce full  $SO(3)$  invariance—*invariant to rotations yet sensitive to reflections*, we include an alignment step that optimally rotates the predicted Zernike spectrum to match the target before computing the loss. This results in a bilevel problem, with the inner loop optimizing a unit quaternion for the best alignment and the outer loop updating the agent model. We compute gradients through the alignment step using implicit differentiation. We perform systematic benchmarking to establish the advantages of our shape-matching loss over other standard distance metrics for shape comparison tasks. We then demonstrate that DiffeoMorph can form a range of shapes—from simple ellipsoids to complex morphologies—using only minimal spatial cues.

In biology, identical cells—each executing the same internal regulatory program—can coordinate to form precise and complex three-dimensional structures [1–3]. These cells interact through a combination of contact-mediated adhesion [4] and long-range signaling (e.g., via diffusible morphogens [5]), yet no cell has global knowledge of the entire system. This raises a fundamental question: how can a single model, shared across all agents, give rise to such intricate collective behavior? This question lies at the heart of developmental biology, and answering it could transform our ability to engineer artificial systems, from self-assembly [6, 7] and swarm robotics [8, 9] to organoids [10, 11].

Machine learning offers a compelling path toward learning such rules automatically, rather than designing them by hand. Two main paradigms have been explored. The first is reinforcement learning (RL), which optimizes decentralized agent policies using reward signals tied to emergent collective behavior [12–14]. RL has been used to train agents to construct predefined shapes and formations [15–18]. However, these methods tend to be inefficient, requiring large amounts of trial-and-error, and do not provide end-to-end differentiability. The second paradigm is end-to-end differentiable learning, where decentralized update rules are trained using gradient descent on a global objective. This approach has been successfully applied through Neural Cellular Automata (NCA) to generate target patterns in 2D [19, 20] as well as 3D grids [21]. Extensions such as Graph NCA [22] and Vision Transformer CA [23] generalize this framework to learn in a continuous space and incorporate attention-based interactions.

However, all of these approaches ultimately rely on comparing a simulated shape to a target shape, and existing formulations, which compare shapes using Cartesian coordinate matrix  $\mathbf{X} \in \mathbb{R}^{N \times 3}$ , suffer from one or more of the following limitations that (1) there are the same number of agents, (2) there exists a point-to-point correspondence, and (3) a simulated shape has the same global orientation as in the target shape. These assumptions are often unrealistic: in natural and engineered multicellular systems, the number of constituent agents may vary, no canonical ordering exists, and the shape may be rotated in an arbitrary way. The shape-matching loss should respect these invariance properties if it is intended for training autonomous morphogenesis rules in realistic settings.

To overcome these limitations, we introduce a spectral shape-matching loss based on the 3D Zernike polynomials [24, 25], which consists of spherical harmonics weighted by radial eigenfunctions. We represent both the generated and target shapes as distributions in space and compare their spectral signatures—the expansion coefficients with respect

---

\* sahand.hormoz@hms.harvard.edu

to Zernike polynomials. Prior approaches that achieve rotation invariance typically remove directional information carried by the azimuthal components. Some do this directly by taking the norm over the azimuthal index  $m$  (as in the power spectrum [25–27]); others combine the coefficients through higher-order angular couplings (as in the bispectrum [28–30] and trispectrum [30]), which also eliminate reflection-sensitive structure in the final representation. In contrast, we retain the full spectral structure and explicitly align the predicted spectrum to the target by optimizing the 3D rotation—parameterized by a unit quaternion—that maximizes their spectral overlap. This design allows the loss to remain rotation invariant while preserving sensitivity to reflection—an essential property for accurately capturing complex morphologies with chirality. Unlike Chamfer [31], Earth Mover’s [32], the pairwise-distance metric (based on comparing all inter-point distances) [33], and Gromov–Wasserstein [34] distances, our loss simultaneously satisfies permutation invariance, point-count robustness, rotation invariance, and chirality sensitivity; unlike power, bispectrum, and trispectrum features, it captures high-frequency shape details; and, despite the alignment step, it achieves superior runtime scaling, since cost depends on the fixed spectral truncation rather than the number of points. These properties, validated through benchmarking experiments, make our loss both expressive and computationally efficient, providing a principled objective for learning 3D morphogenesis.

We combine this novel shape-matching loss with an SE(3)-equivariant force model to introduce **DiffeoMorph**, an end-to-end differentiable framework for learning morphogenesis control that drives agents to collectively form target 3D shapes. During simulation, the force model updates each agent’s position and internal states based on its current configurations and the signals received from other agents. Because the loss internally optimizes the alignment between the predicted and target Zernike spectra, each gradient step over model parameters requires solving the alignment optimization problem. This dependency yields a bilevel optimization structure: the outer loop updates the agent model, while the inner loop solves for optimal spectral alignment. We compute gradients through the inner loop using implicit differentiation, enabling efficient end-to-end training without unrolling the alignment process. We demonstrate that, starting from an uninformative spherical configuration with only minimal spatial cues encoded in the agents’ internal states, DiffeoMorph can robustly generate a range of complex 3D shapes. Overall, DiffeoMorph provides a general framework for learning distributed control strategies for morphogenesis, swarm robotics, and programmable self-assembly.

## RESULTS

### Overall framework

DiffeoMorph comprises two stages: morphogenesis simulation and shape matching (Fig. 1a). Drawing inspiration from biological cells, we represent the internal state of each agent  $i$  using a gene expression profile  $\mathbf{g}_i$  and an orientation vector, referred to as its polarity  $\mathbf{p}_i$ . In the morphogenesis stage, the position of each agent is updated by a learnable control protocol based on its internal state. We formulate this control using a model based on an SE(3)-equivariant architecture called Equivariant Graph Neural Networks [35] in which each agent senses its neighborhood through pairwise messages between the agents. These messages depend on the squared pairwise distance  $d_{ij}^2$ , the relative angle  $\theta_{ij}$  of the polarization vectors  $\mathbf{p}_i$  and  $\mathbf{p}_j$ , and the respective gene expressions  $\mathbf{g}_i$  and  $\mathbf{g}_j$  of agents  $i$  and  $j$ . Since gene expression vectors are rotation invariant and polarity vectors enter only through their pairwise angle, the resulting message remains rotation invariant as well. To make neighborhood sensing more adaptive, we employ an attention mechanism [36], computing attention coefficients  $\alpha_{ij}$  from the same edge features used to form the messages. The model also computes an equilibrium length that specifies an optimal separation distance between agents. These quantities are used together to compute the forces governing position, gene expression, and polarity updates,  $\mathbf{F}_{(\mathbf{x}/\mathbf{g}/\mathbf{p})_i}$  (see ‘Morphogenesis Model’ section in the Methods). By iteratively recomputing the forces from the updated agent states and integrating them forward in time under noise with a Neural differential equation solver [37–39], we obtain the morphogenesis trajectory that is differentiable end-to-end.

The second stage is shape matching. In this step, we must compare the evolved shape with a target shape where point-to-point correspondence is unknown, the number of points differs, and the global orientation is not aligned. We address this challenge by viewing a point cloud as a discrete approximation of a smooth function over space, which can be expanded in a suitable basis. To this end, we normalize each point cloud to lie within the unit ball and project it onto the 3D Zernike polynomials—which form the eigenbasis of the unit ball—to obtain the 3D Zernike moments  $\mathbf{C} := \{c_{n\ell m}\}$  of radial order  $n$ , angular degree  $\ell$ , and azimuthal index  $m$ . Collectively, we refer to these coefficients as the spectrum of the shape. Because the azimuthal component  $m$  depends on the orientation of the shape with respect to the coordinate axes, we align the spectrum of the evolved shape,  $\mathbf{C}^{\text{evol}}$ , to that of the target,  $\mathbf{C}^{\text{target}}$ . We do this by maximizing the spectral overlap between the two spectra,  $\mathcal{M}(\mathbf{C}^{\text{evol}}, \mathbf{C}^{\text{target}})$ , defined as the inner product of their Zernike moments after rotating the evolved spectrum. To represent this rotation, we parameterize it with a unit quaternion  $\mathbf{q}$ , which determines the corresponding Wigner–D matrices  $D^\ell(\mathbf{q})$  acting on the azimuthal indices at

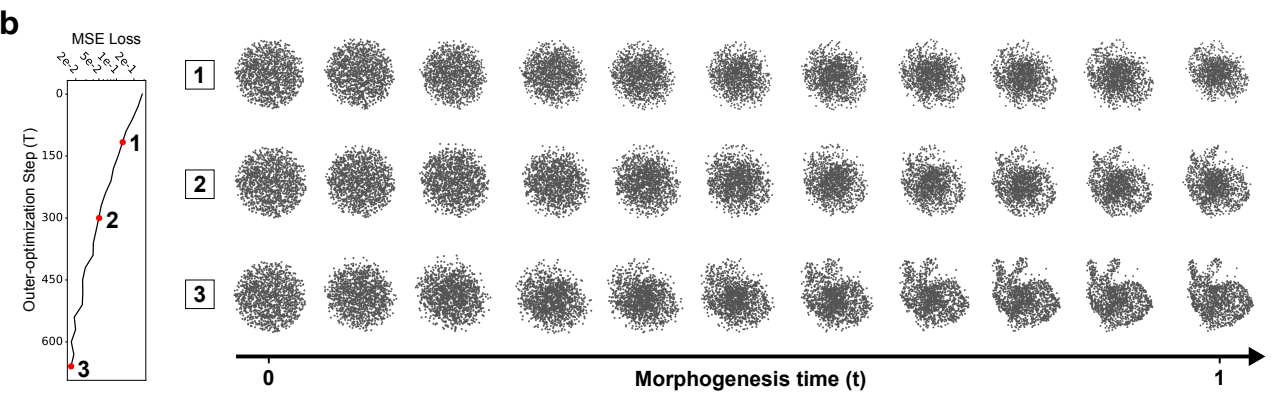
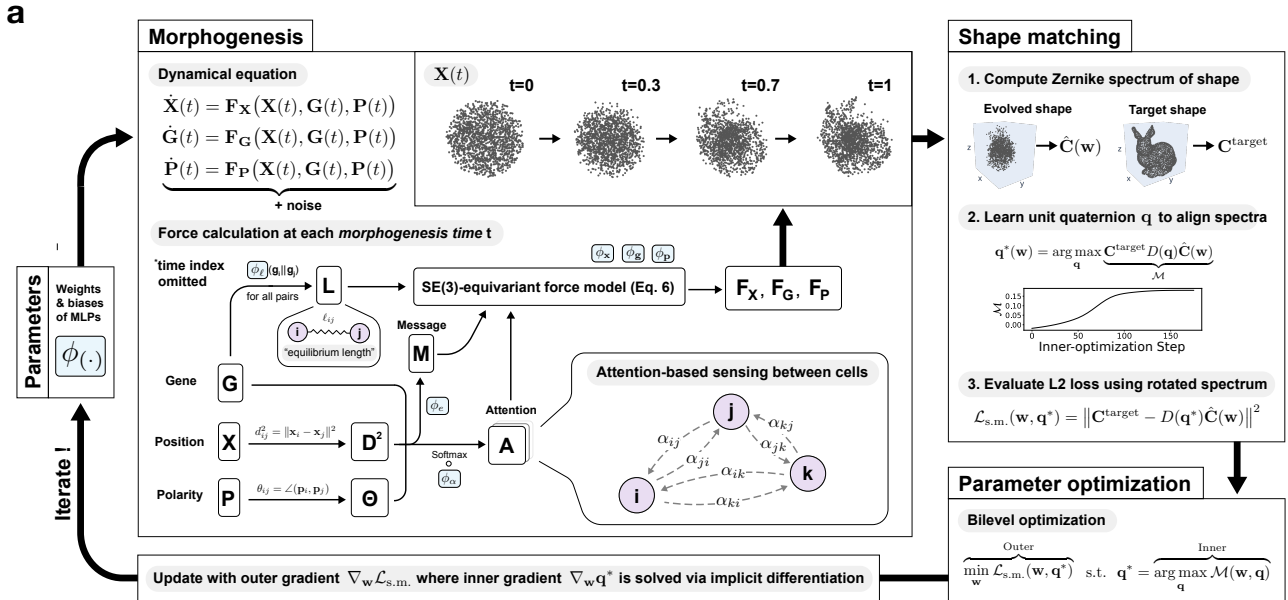


FIG. 1. Overview of the morphogenesis model and shape optimization of DiffeoMorph. (a) Agents sense their neighbors using an attention-based mechanism based on distances to neighbors as well as their internal states. The force model evolves the positions of agents and internal states, without direct access to positions of neighbors. The final evolved shape is compared to a target shape using their spectra given by the 3D Zernike moments. A bilevel optimization procedure aligns the spectra by learning the unit quaternion (inner optimization) and updates model parameters to minimize the shape-matching loss (outer optimization) (b) As the outer optimization proceeds, the simulation produces a desired target shape.

degree  $\ell$ . Since no closed-form solution exists for the rotation that maximizes this overlap, we learn  $\mathbf{q}$  via gradient descent. Once the best alignment is found, we compute the mean squared error (MSE) between the aligned spectra. This intermediate alignment step ensures that the MSE is evaluated under the best orientational match, thereby making the shape-matching loss  $\mathcal{L}_{\text{s.m.}}$  rotation invariant.

Together, the projection onto the 3D Zernike polynomials and the subsequent spectral alignment provide a well-defined loss that compares two shapes up to rotation. Incorporating this loss into the learning of the morphogenesis model introduces an additional layer of structure. Let  $\mathbf{w}$  denote the parameters of the morphogenesis model. The intermediate spectral alignment optimization makes the shape-matching objective a bilevel problem: the outer problem of learning  $\mathbf{w}$  requires solving the inner problem of finding the optimal unit quaternion  $\mathbf{q}^*$  for spectral alignment. Differentiating the shape-matching loss  $\mathcal{L}_{\text{s.m.}}$  with respect to  $\mathbf{w}$  therefore requires the inner gradient  $\nabla_{\mathbf{w}}\mathbf{q}^*$ . Although this term can be obtained either by backpropagating through the iterative gradient-based optimization of the spectral alignment or by solving the corresponding adjoint equation backwards, both approaches are computationally expensive in terms of both memory and time. We instead compute this term efficiently using implicit differentiation (see ‘Shape-matching loss’ section in the Methods for details). Since the morphogenesis simulation is itself differentiable, we optimize the model parameters with the outer gradient  $\nabla_{\mathbf{w}}\mathcal{L}_{\text{s.m.}}$ . The morphogenesis model progressively learns to reproduce the target shape (Fig. 1b).

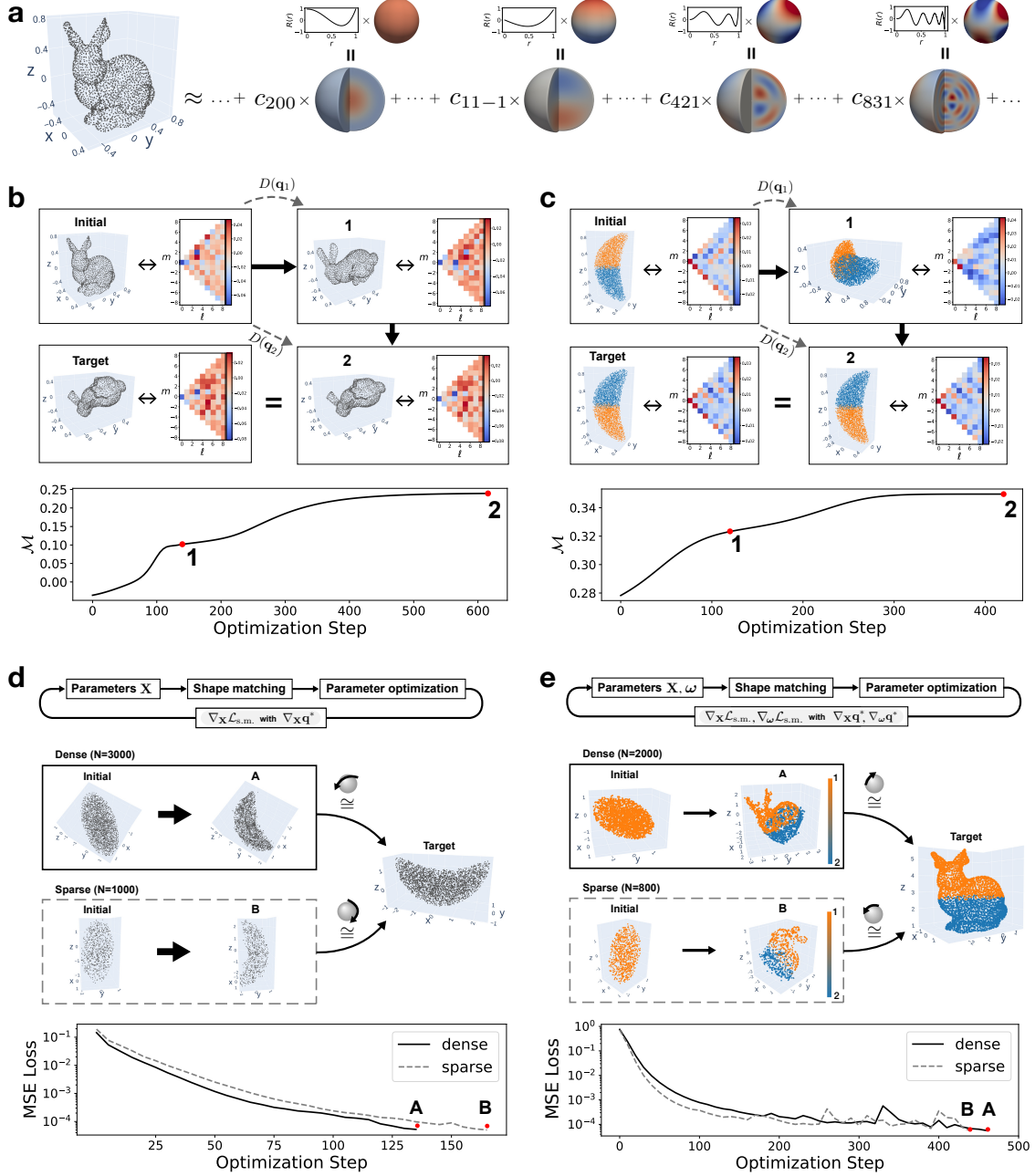


FIG. 2. Spectral alignment and shape optimization by matching 3D Zernike moments. (a) A 3D shape represented as a point cloud can be expressed as a linear combination of the 3D Zernike polynomials, composed of radial and angular parts. The expansion coefficients  $\mathbf{C} := \{c_{nlm}\}$  are the Zernike moments. (b) The spectra of two shapes, given by the Zernike moments, can be aligned by solving for the unit quaternion that maximizes the spectral overlap  $\mathcal{M}$ . When the optimization converges at point 2, the corresponding unit quaternion  $\mathbf{q}_2$  rotates, via the Wigner-D matrix  $D$ , the spectrum of the standing bunny in the Initial box to align with that of the toppled bunny in the Target box. Spatially rotating the point cloud using the corresponding spatial rotation matrix yields identical orientation to the target. (c) The same experiment is performed on weighted point clouds, with orange and blue indicating weight values of 1 and 2, respectively. Applying the spatial rotation corresponding to the optimized unit quaternion flips the crescent by 180°, placing the regions with weight 1 and weight 2 on the correct arms to match the target configuration. (d, e) To isolate the behavior of the shape-matching loss, we bypass the simulation step and directly optimize the input point cloud  $\mathbf{X}$  in (d) and, along with its weights  $\omega$ , in (e). Solving the resulting bilevel optimization problem successfully morphs both dense and sparse ellipsoidal point clouds—each with a different initial orientation—into the target shapes. Importantly, the optimization cares only about matching morphology, not absolute orientation, highlighting the rotation invariance of the loss.

## Spectral alignment and shape learning with Zernike moments

Because the shape-matching loss of DiffeoMorph can be integrated with any force model—or even used in different learning paradigms such as RL, we begin by decoupling the learning problem from the simulation component of DiffeoMorph to evaluate the behavior of our loss in a more controlled setting.

We first designed proof-of-concept experiments to test whether the rotation that aligns two shapes in spectral space can be learned directly by gradient descent (the inner optimization problem). We parameterize this rotation by a unit quaternion  $\mathbf{q}$ , which provides a smooth, singularity-free representation of 3D rotations and avoids the gimbal-lock issues inherent to Euler angles. As test shapes, we used an unweighted point cloud of Stanford bunny and a weighted point cloud in the shape of crescent, both normalized to lie within the unit ball. The point cloud in each half of the crescent is assigned a weight 1 and 2, respectively (shown as orange and blue color in Fig. 2c). In Fig. 2a, we first visualize a few terms of the expansion of the bunny, in the order of increasing complexity of the 3D Zernike polynomials, to further illustrate the passing from the Euclidean representation to the spectral representation. The expansion coefficients, Zernike moments  $\mathbf{C}$ , up to angular degree  $\ell=8$  are shown as a matrix in Fig. 2b,c at a fixed radial order  $n=1$ . The goal is to find the optimal unit quaternion  $\mathbf{q}$  whose Wigner-D matrices  $D^\ell$  align the Zernike moments of the upright bunny (crescent) shown in the “Initial” box to those of the toppled bunny ( $180^\circ$ -rotated crescent) in the “Target” box.

As the spectral alignment progresses from point 1 to point 2 in Fig. 2b, the predicted spectrum rotates to match the target. Applying the corresponding spatial rotation matrix  $R$  to the point cloud yields the toppled bunny. A similar alignment occurs for the weighted crescent in Fig. 2c. Notably, only the odd- $\ell$  components change substantially—consistent with the 2-fold cyclic symmetry of the crescent, under which odd- $\ell$  spherical harmonics flip sign while even- $\ell$  terms remain invariant. These results demonstrate the inner optimization can learn the optimal  $\mathbf{q}$  by maximizing the spectral overlap  $\mathcal{M}$ .

Next, we designed proof-of-concept experiments to validate whether the inner gradient through the spectral alignment step can be correctly computed using implicit differentiation. To isolate this step from the rest of the pipeline, we bypass the morphogenesis simulation shown in Fig. 1a and treat the structure—the point cloud  $\mathbf{X}$  and, when present, its weights  $\omega$ —as directly optimizable parameters, as illustrated in the top row of Fig. 2d,e. We then minimize the shape-matching loss  $\mathcal{L}_{\text{s.m.}}$  by computing its gradient with respect to inputs, i.e.,  $\nabla_{\mathbf{X}}\mathcal{L}_{\text{s.m.}}$  alone or jointly with  $\nabla_{\omega}\mathcal{L}_{\text{s.m.}}$ . This experiment remains relevant to the full DiffeoMorph framework, as optimizing the agent model parameters ultimately involves backpropagating through  $\mathbf{X}$  via the chain rule:  $\nabla_{\mathbf{w}}\mathcal{L}_{\text{s.m.}} = \nabla_{\mathbf{X}}\mathcal{L}_{\text{s.m.}} \cdot \nabla_{\mathbf{w}}\mathbf{X}$ , plus an additional  $\nabla_{\omega}\mathcal{L}_{\text{s.m.}} \cdot \nabla_{\mathbf{w}}\omega$  term if  $\omega$  is included. The goal in this setup is to morph two initial point clouds shaped as ellipsoids—each differing in orientations and number of agents—into a target shape that has a different morphology, number of agents, and, when present, weight distribution.

The bottom row of Fig. 2d,e plots the MSE between the Zernike moments of the evolving shapes and the target. At convergence, both point clouds—denoted by points “A” and “B”—successfully replicate the crescent and bunny morphologies, respectively, despite retaining the global orientations of their initial ellipsoids. This illustrates the rotation invariance of our objective: optimization converges once the correct morphology (and weight distribution) is recovered up to rotation. The inner optimization—visualized by the 3D rotation glyph—correctly aligns the predicted and target spectra, achieving low MSE even when the raw point clouds differ by rotation. Together, these results validate that our loss is invariant to both global orientation and point count, while demonstrating that the gradients required for optimization can be accurately computed via implicit differentiation. We demonstrate the computational speedup achieved by implicit differentiation relative to direct backpropagation in Supplementary Information Section 9.

## Benchmarking shape-matching objective

Since the shape-matching loss in DiffeoMorph is a key contribution, we perform several benchmarking experiments to highlight its advantages over standard distance metrics for shape comparison. For comparison, we use Chamfer [31] (nearest-neighbor matching), Earth Mover’s [32] (optimal transport between point sets), Pairwise [33] (comparison of inter-point distance matrices), Gromov–Wasserstein [34] (optimal transport that matches pairwise distances), Power Spectrum [25–27] (rotation-invariant magnitudes of Zernike coefficients), bispectrum [28–30] (third-order rotation-invariant couplings of angular modes), and trispectrum [30] (fourth-order rotation-invariant couplings with higher geometric detail). The mathematical expressions for these distances are provided in Supplementary Information section 11.

In Fig. 3a, we compute the distances between the bunny point cloud and several geometrically perturbed variants. We also include the comparison against itself (Self) to establish a baseline value for each metric. The nonzero Self-to-Self distances for Earth Mover’s and Gromov–Wasserstein distances arise from the entropic regularization used to relax the optimal transport problem into a smooth, differentiable objective [40, 41]. Chamfer and Earth Mover’s

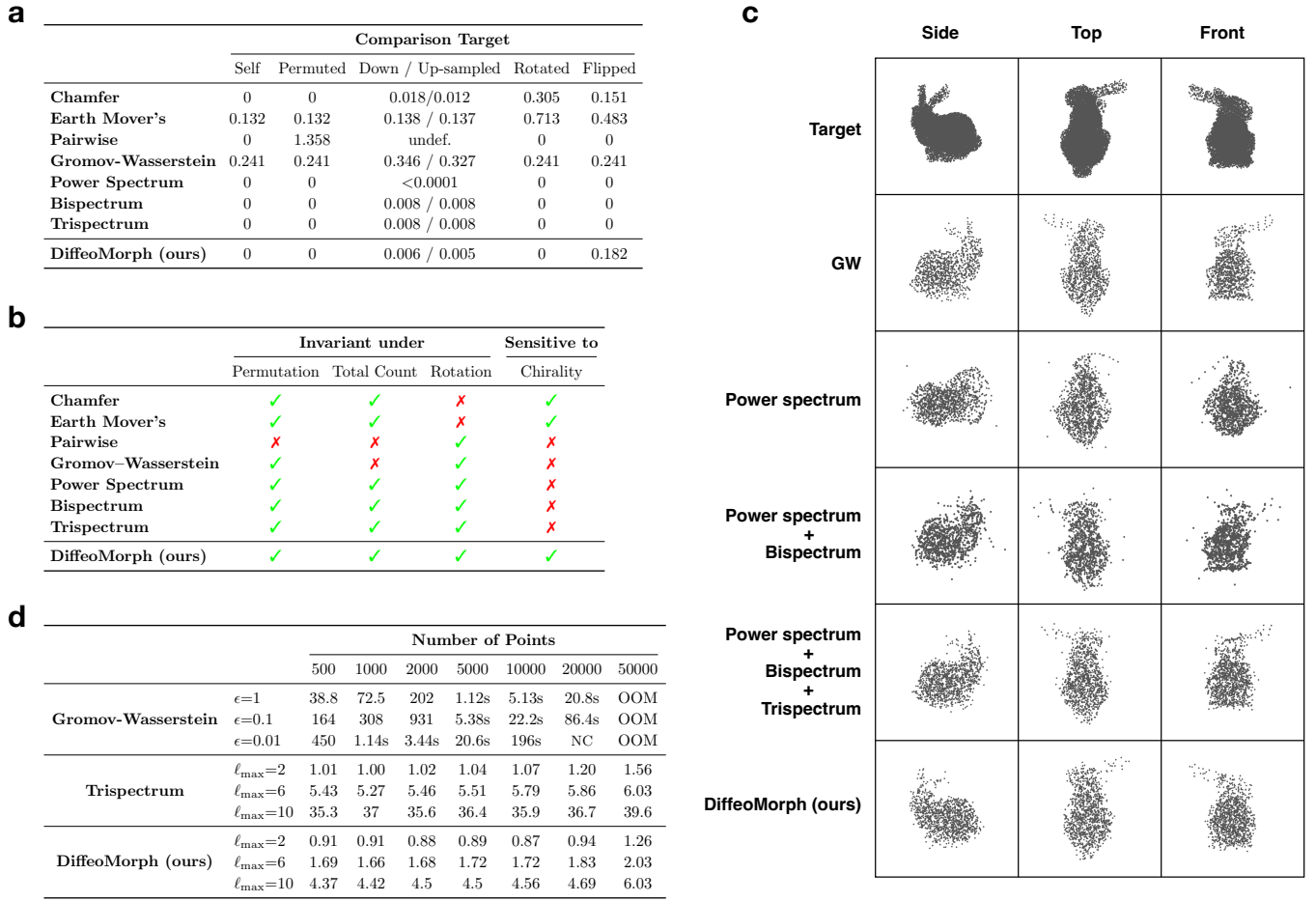


FIG. 3. Benchmarking the proposed loss. (a) Distances between the original bunny point cloud (Self) and its geometrically perturbed variants are computed using standard losses for shape comparison. For optimal transport-based losses (Earth Mover's and Gromov-Wasserstein), the distances between identical shapes (Self vs. Self) are nonzero due to the probabilistic relaxation introduced by the entropic regularization, which is required to make them differentiable. (b) Behavior of each loss summarized based on (a). Our loss is the only distance metric satisfying all desired properties. (c) Visualizations of point clouds learned through the direct shape optimization setup of Fig. 2d using losses satisfying the three invariance properties. We compute higher-order spectra cumulatively: the bispectrum includes the power spectrum, and the trispectrum includes both the power spectrum and bispectrum. The correct head direction is recovered only when training with our loss. (d) Runtime analyses. Gromov-Wasserstein distance scales poorly with the number of points and the weakening of regularization, captured by decreasing  $\epsilon$ . In contrast, the runtime of the spectra-based losses is unaffected by the number of points, since the summation over points during projection step is vectorized. However, computing the trispectrum is slower than our loss because it requires enumerating valid quartets of angular degrees ( $\ell_1, \ell_2, \ell_3, \ell_4$ ) to capture fourth-order coupling. The spectral alignment step in our loss is faster than this enumeration process, even when vectorized, resulting in the best overall runtime performance.

distances compare two point clouds by allowing any point in one cloud to match to any point in the other—via nearest-neighbor matching for Chamfer and via an optimal transport plan for Earth Mover's—rather than relying on a fixed  $i$ -to- $j$  correspondence. This flexibility makes them invariant to permutations of the points and able to handle point clouds of different sizes. However, they are sensitive to rotation: rotating the target yields a large distance because the comparison is made directly on raw coordinates. Pairwise distance addresses this issue by comparing distances within each point cloud,  $\|\mathbf{x}_i - \mathbf{x}_j\| - \|\mathbf{y}_i - \mathbf{y}_j\|$ , which makes it rotation invariant. However, it is sensitive to index permutation and total count because it requires an explicit point-to-point correspondence. Gromov-Wasserstein distance combines the strengths of both approaches by finding the optimal probabilistic coupling  $\pi_{ij}$  that minimizes discrepancies between all pairwise distances across two point clouds. As a result, it yields the same value for permuted and rotated point clouds as in the Self comparison. However, changes in the number of points affect the coupling pattern in  $\pi_{ij}$ , making the metric sensitive to total point count. The spectral metrics avoid these issues entirely. The power spectrum is obtained by summing the squared magnitudes of the 3D Zernike moments over the azimuthal

index  $m$ , yielding a single energy value for each angular degree  $\ell$ . This summation removes the directional information encoded in the  $m$ -components and therefore discards substantial geometric detail. The bispectrum and trispectrum retain more structure by coupling pairs and quartets of angular degrees, respectively, to form rotation-invariant descriptors. Although these higher-order spectra capture finer geometric correlations than the power spectrum, they remain reduced representations of the full  $(\ell, m)$ -dependent Zernike moments, and thus lose information relative to them. As a consequence of their construction, the power spectrum, bispectrum, and trispectrum all become insensitive to reflections and therefore cannot distinguish chiral configurations. Only Chamfer and Earth Mover’s distances—which compare the raw coordinates of the point clouds—and our loss, which retains the azimuthal components, are sensitive to reflection. These properties are summarized in Fig. 3b. Among the metrics considered, only our loss simultaneously satisfies all four desired criteria for shape matching: invariance to point permutations, robustness to differing point counts, invariance to rotations, and sensitivity to chirality.

To understand how these properties affect learning, we performed the direct shape learning task of Fig. 2d with Gromov–Wasserstein distance (shown as GW) and the spectrum-based metrics. The learned shapes obtained using each metric are rotated to align with the target shape and are visualized together in Fig. 3c. Optimization with GW and with all three rotation-invariant spectral metrics can reproduce the target bunny shape, but only up to reflection. Because a reflection-invariant metric cannot distinguish a shape from its mirror image, the optimization has no way to prefer one head orientation over the other. As a result, the learned bunny may emerge facing either direction, depending solely on the initial configuration of the ellipsoid. We also find the power spectrum alone, or even in combination with the bispectrum, lacks expressive power to capture fine geometric details such as the bunny’s ears. This suggests that fourth-order coupling through the trispectrum is necessary for accurate shape reconstruction. Our loss, by preserving azimuthal information, successfully recovers the bunny with high fidelity and the correct head orientation.

In Fig. 3d, we benchmark the evaluation runtime of Gromov–Wasserstein distance, Trispectrum (alone) and our loss. All values are reported in milliseconds. Gromov–Wasserstein scales poorly with increasing point count  $N$  because each iteration requires manipulating full  $N \times N$  matrices and repeatedly forming products between them, leading to quadratic memory usage and cubic computational cost. Notably, it reaches an out-of-memory error (denoted OOM) at  $N=50000$  because iorithm stores the coupling matrix and two pairwise distance matrices, each of size  $N \times N$ . Lowering the regularization parameter  $\epsilon$  slows the algorithm because the Sinkhorn updates require many more iterations to converge. The trispectrum and our loss do not scale with  $N$  since the point cloud is first projected onto Zernike polynomials and subsequently handled via Zernike moments. Increasing the number of angular components  $\ell_{\max}$  increases the runtime in both cases, but to different degrees. The trispectrum’s  $\ell_{\max}$ -scaling is due to enumerating quartets of angular degrees  $(\ell_1, \ell_2, \ell_3, \ell_4)$  that satisfy the selection rules. In contrast, DiffeoMorph’s runtime grows more slowly because the dominant cost comes from evaluating Wigner–D matrix for each  $\ell$ , which can be efficiently vectorized. Therefore, even with the intermediate spectral alignment, our loss achieves the most competitive runtime. Taken together, these results show that our shape-matching loss uniquely combines the geometric invariances, expressive power, and computational efficiency needed for reliable 3D shape learning.

### Morphing into target shapes via agent-based simulation

To demonstrate the full capabilities of DiffeoMorph, we evaluated its performance in morphing a population of agents into a range of complex 3D target shapes: an ellipsoid, a crescent, and the Stanford bunny (Fig. 4a). The agents were evolved using the  $SE(3)$ -equivariant force model. Before presenting results, we highlight a key design consideration. If each agent were initialized with a unique internal state—for example, by encoding its spatial coordinates  $[x_i, y_i, z_i]$  or any other agent-specific identifier—and if the morphogenesis simulation contained no noise, then a simple MLP acting independently on each agent could trivially learn a pointwise mapping from the initial cloud to the target. In this regime, morphogenesis degenerates into supervised coordinate regression and requires no communication or collective behavior.

To avoid this trivial regime and make the task biologically and algorithmically meaningful, we deliberately obfuscate both spatial and internal information. Taking inspiration from developmental biology—where most morphogenesis begins from a nearly spherical aggregate of cells—we initialize the population as an approximately uniform sphere. The shell is generated using the Fibonacci lattice [42] to ensure close to uniform sampling, and the interior is filled using Poisson-disk sampling [43], producing a point cloud with a uniform shell and mild spatial disorder in the core. Onto this sphere, we impose a minimal patterning cue: a polar region consisting of  $N_{\text{org}}$  nearest-neighbor cells on the shell is designated as an organizer region and is made to uniformly express a single gene that is off in all other cells. We motivate this setup by the localized expression of morphogens at a pole [44, 45] or the classical Spemann organizer [46, 47], which establishes the body axis in early development. We then elongate the sphere by 10% along the axis passing through this organizer. When introducing additional organizer groups, they are placed 90° apart from the

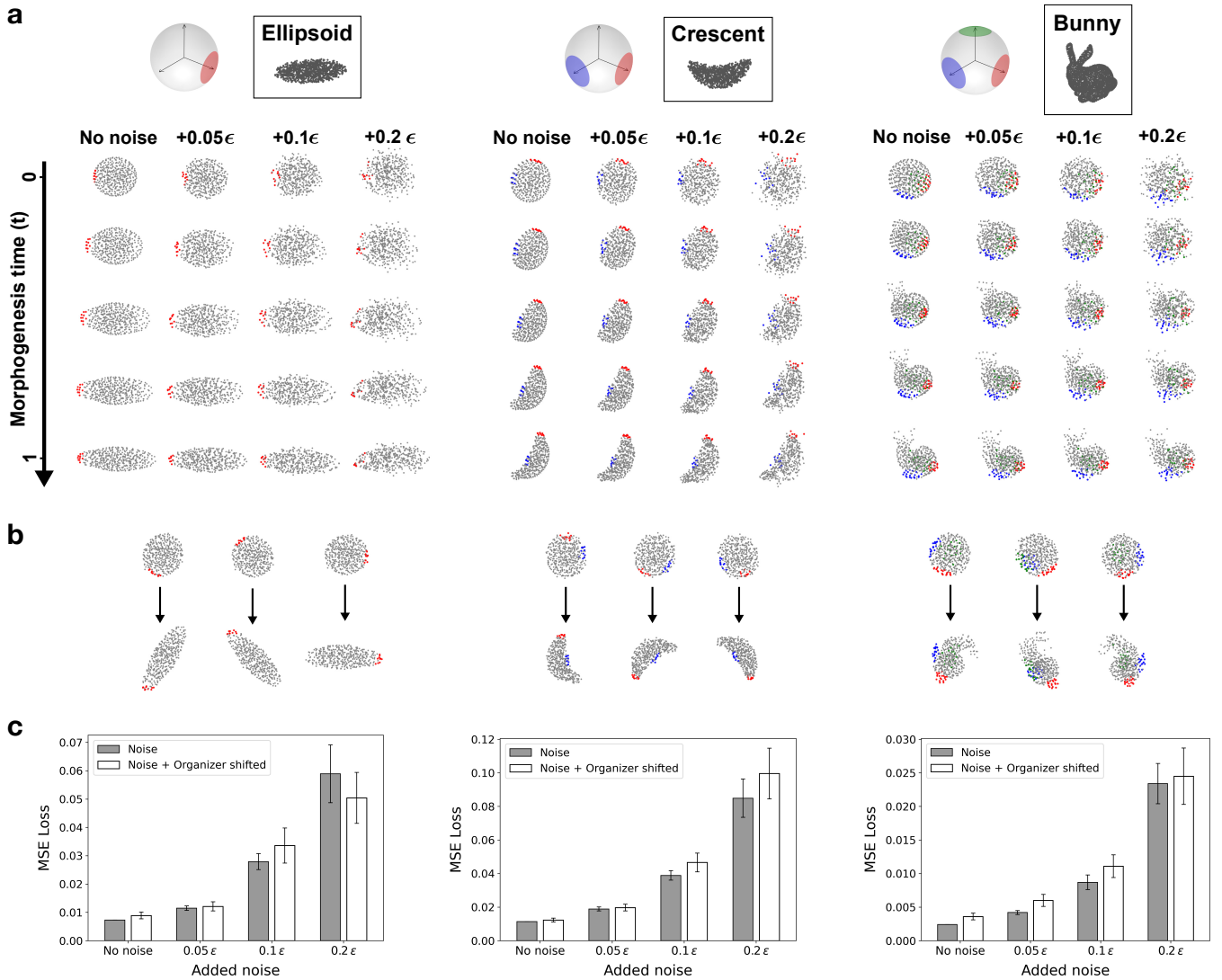


FIG. 4. Visualization of morphogenesis trajectories from trained models. (a) The ellipsoid, crescent, and bunny serve as representative shapes with successive stages of symmetry breaking. Colored regions indicate “organizer cells,” within which cells share the same gene expression pattern distinct from the rest. When introducing an additional group of organizer cells, each new group is assigned a different pattern and placed orthogonally to the preexisting group(s). Models—trained at noise magnitudes of  $0.05\epsilon$  (ellipsoid and crescent) and  $0.03\epsilon$  (bunny)—maintain robust morphogenesis trajectories, preserving overall geometries even under higher noise levels. (b) Shifting the organizer regions, while keeping the coordinates of cells fixed, results in a new morphogenesis whose global orientation is shifted accordingly. (c) Generalization under added noise with and without organizer shifts. Increasing noise levels leads to higher test losses, consistent with trajectories shown in (a), while shifting the organizers causes only a moderate increase across all shapes.

previous axis (with the third axis determined by the right-hand rule), and each group is assigned a different gene that is expressed uniformly within that organizer and off elsewhere. This procedure yields one to three discrete agent types—shown as colored regions in Fig. 4a—that seed the patterning process. All polarity vectors  $\mathbf{p}_i^0$  are initialized to point along the same random direction. Further details of the initialization procedure are provided in ‘Preparation of initial states’ section in the Methods. In this setup, agents must infer their spatial context from limited internal cues. Without communication, this is impossible: the internal state alone carries no positional information. As a result, successful morphogenesis demands decentralized coordination: agents must decode spatial information from aggregated signals and then use it to collectively morph into the target shape.

At each training step, we further perturb the initial positions with zero-mean Gaussian noise of magnitude 0.05 for the ellipsoid and crescent experiments and 0.03 for the bunny experiment. Together with the imposed elongation, these perturbations intentionally break the rotational symmetry of the initial sphere. While such symmetry is common

in early embryos and is not biologically restrictive, it poses a significant computational challenge for our method. As detailed in Supplementary Information section 3, the implicit differentiation of the spectral alignment step requires inverting a Hessian defined on the rotation parameters. For a perfectly rotationally symmetric shape, this Hessian becomes singular: all rotations around the symmetry axis leave the spectrum unchanged, producing a continuum of equivalent optima. By introducing mild asymmetries through elongation and noise, we lift this degeneracy and ensure that the Hessian remains well-conditioned and invertible. This is a striking instance in which a purely computational requirement—stable gradient propagation—imposes a symmetry breaking that is not required by the underlying physical system.

Following training, we test the learned force model under stronger perturbation by increasing the noise magnitude up to 0.2 (Fig. 4a, top-to-bottom trajectory) and by shifting the positions of organizer regions while keeping the point cloud fixed (Fig. 4b, visualized for  $0.05\epsilon$ ). Note that the Poisson-disk sampling introduces spatial nonuniformity to the core; therefore, once the organizers are shifted, spatial cues from the shell must be propagated by the agents arranged differently in space. As the initial perturbation increases, the final point clouds become less sharply defined, with some agents located away from the main body, but DiffeoMorph consistently recovers the overall geometry, with the resulting orientation determined by the locations of the organizer cells. For instance, the crescent’s curved shape and the separation between the bunny’s blobby body and the face with pointed ears are reproduced even when initial point clouds are severely perturbed—so much so that the inner–outer arrangement between the core and shell is disrupted, with some core cells bulging outward. We summarize generalization performance in Fig. 4c based on 10 independent noise realizations (and an additional 10 random orientations per noise realization for the organizer-shift experiment). These results indicate that the learned force model captures a morphogenesis protocol that generalizes well across diverse initial configurations. In Supplementary Information Section 10, we benchmark the model against Graph Neural Cellular Automata models and find that our model achieves the best performance.

### Analyses of morphogenesis process

To better understand how the model learns to produce robust morphogenesis, we analyze the trajectories of gene expression patterns and polarity vectors (Fig. 5a). We focus on representative genes that are initially turned off for all cells. The top row corresponds to  $t=0.05$ , since at  $t=0$  these genes have zero expression and polarity vectors are uniformly aligned. When visualized spatially across the cell population, these genes exhibit striking domain-like patterns reminiscent of coordinate-setting gene expression in early embryonic development [48, 49]. For the ellipsoid, genes develop high- and low-expression regions that distinguish the poles from midsection. A similar spatial organization appears in the crescent example, with the additional feature that Gene 23 displays distinct expression levels between the inner and outer regions of the curved shape—analogous to how genes in the BMP pathway (e.g., chordin or bmp4) establish dorsal-ventral symmetry breaking during early embryogenesis [50]. In the bunny, expression patterns become more structured as genes evolve, seemingly demarcating specific morphological compartments. Interestingly, these domains develop non-monotonically; for instance, the midline between the face and body initially shows low expression of Gene 14 but later switches to a high-expression state. Polarity vectors exhibit a similar domain-specific pattern, where those belonging to the same body parts are aligned.

Drawing an analogy to biological gene expression, we visualize the learned gene expressions using UMAP, jointly embedding all time points into a shared 2D coordinate space—a standard approach in single-cell RNA sequencing [51] (Fig. 5b). To help track the temporal evolution of individual cells, we connect their UMAP locations across snapshots. We then cluster the final-time embeddings (highlighted as red points and enclosed by a black boundary line) using the Leiden algorithm and map the resulting cluster identities as different colors onto both the UMAP space and the spatial coordinates of the cells. We use the same set of parameters for all three shapes (see ‘Details of experimental setup’ section in the Methods). The results clearly show that different gene expression profiles, corresponding to different clusters, mark distinct spatial regions of the shapes. Comparing these patterns reveals how distinct gene expression zones emerge based on morphology. For instance, the midsection of the ellipsoid forms a single cluster (blue), whereas in the crescent this same region separates into two distinct clusters (green and orange), effectively marking the dorsal and ventral sides. Similarly, the bunny exhibits a more intricate spatial distribution of clusters. These results suggest that agents learn to encode positional identity and spatial domains into their internal state, effectively creating a coordinate system to guide complex morphogenesis.

## DISCUSSION

In this study, we presented DiffeoMorph, an efficient end-to-end differentiable framework for guiding a population of agents to self-organize into target 3D shapes. DiffeoMorph consists of a novel 3D Zernike moment-based shape-

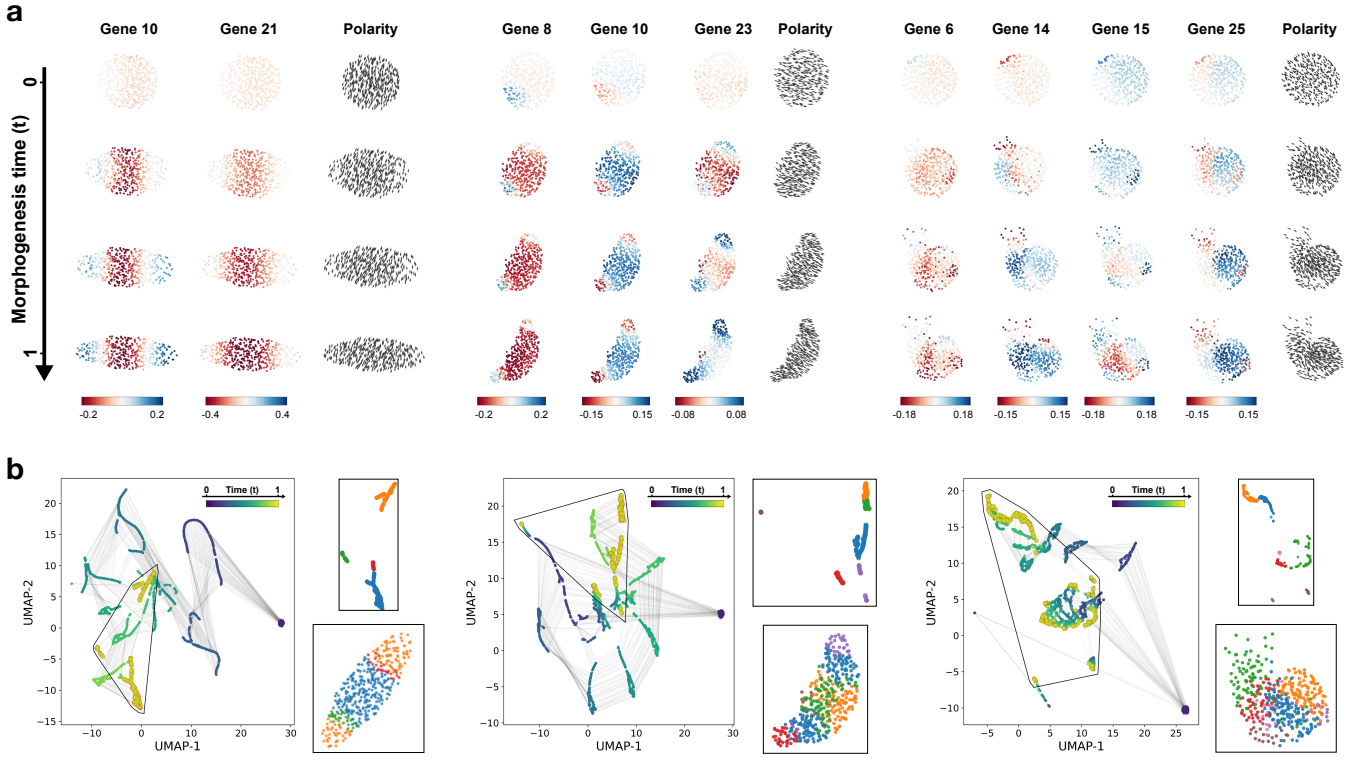


FIG. 5. Visualization of the evolution of internal states during morphogenesis. (a) Expression patterns of representative genes and polarity (shown as arrows). The top row corresponds to  $t=0.05$ . As morphogenesis proceeds, gene expression levels develop spatial variation, jointly encoding distinct regions of the shape, while polarity vectors evolve coherently with these domains. (b) UMAP visualization of gene expression trajectories (left); gray lines connect the same agent across time points to track its evolution. Final-time embeddings (highlighted as points enclosed by black boundary lines) are clustered using the Leiden algorithm, and the resulting cluster identities are mapped onto the final spatial shape (insets). Distinct clusters mark different spatial domains.

matching objective to compare two point clouds in a manner invariant to permutation, number of points, and global orientation, while remaining sensitive to reflections. We confirm this property as well as runtime advantage from extensive benchmarking. We pair the loss with an  $SE(3)$ -equivariant force model—extended from EGNN architecture to incorporate attention mechanism and physical quantities such as equilibrium length—that can learn a generalizable morphogenesis control protocol based on minimal spatial cues. We demonstrate the capacity of the overall framework by successfully forming various shapes with increasing morphological complexity.

A potential limitation of the shape-matching objective is that its intermediate spectral alignment problem may have local optima, particularly when comparing two complex shapes with high-frequency modes. This issue is mitigated in our morphogenesis experiments thanks to the gradual emergence of morphological details. Early in training, alignment is performed with an under-developed, blobby shape containing only low-frequency modes. By warm-starting the alignment at each step from the previous orientation, we can gradually refine the alignment as high-frequency modes develop during morphogenesis without getting stuck in a poor local optimum. In contrast, this advantage is absent when comparing two fully formed shapes from the outset (e.g., clustering shape datasets). In such cases, additional strategies, such as progressively fine-tuning the alignment from low- to high-frequency modes, may be required.

A key limitation of the force model is that it is parameterized with generic neural networks rather than biologically realistic mechanisms for sensing, signaling, and internal state dynamics. Although the design is intentionally general—for instance, the same internal-state logic could be readily implemented in swarm robots—and biological systems serve only as inspiration, this abstraction limits the ability to draw meaningful connections to real developmental processes. Incorporating more biologically realistic components, such as gene regulatory networks [52, 53], actomyosin-driven directional mechanics [54], cadherin-mediated adhesion forces [55], or additional external fields such as ions to capture bioelectric phenomena [56] or internal cell type to represent context-sensitive differentiation [57, 58] would make the framework more interpretable and better suited for modeling biological morphogenesis.

Future extensions include integrating such biological realism [18, 59–61], and extending the learning task to enable systems to not only form shapes but also recover them from perturbations through self-healing [62–64]—hallmarks of

robust developmental programs in nature. We can also utilize transfer learning to adapt a pretrained model across different target shapes, which raises an interesting question about which shape distributions are optimal for pretraining so the model can generalize efficiently to novel morphologies [65]. Learning dynamical behaviors such as undulatory locomotion [66, 67] would also be a promising direction. By turning the design of morphogenesis programs into a differentiable optimization problem, DiffeoMorph offers a unified way to design and interrogate self-organizing systems across biology, robotics, and programmable matter.

## METHODS

### Morphogenesis Model

#### *Internal State of an Agent*

Drawing inspiration from biological cells, we represent the internal state of each agent  $i$  using two components: a  $d_g$ -dimensional gene expression vector  $\mathbf{g}_i \in \mathbb{R}^{d_g}$  and a polarity vector  $\mathbf{p}_i \in S^2$ . Across the population, these are aggregated into matrices  $\mathbf{G}$  and  $\mathbf{P}$ , respectively, and evolve together with the position matrix  $\mathbf{X}$  during the morphogenesis simulation (Fig. 1a). The gene expression vector  $\mathbf{g}_i$  encodes rotation-invariant internal features, while the polarity  $\mathbf{p}_i$  defines an equivariant direction in 3D space. To ensure that polarity vectors remain on the unit sphere throughout the simulation, we normalize  $\mathbf{p}_i$  after each update.

At each time step  $t$ , the system is described by the positions of the agents  $\mathbf{X}^t$  and internal states  $\mathbf{G}^t$  (gene expression vectors) and  $\mathbf{P}^t$  (polarities). For clarity, we omit the time index  $t$  in what follows.

#### *SE(3)-equivariant force model*

To evolve the positions and states of agents in a manner consistent with rigid body transformations, we employ an SE(3)-equivariant EGNN [35] to compute forces for time integration.  $\phi(\cdot)$  in the description below denotes a multi-layer perceptron (MLP) and  $\mathbf{w}$  collectively refers to their learnable parameters.

For each pair of agents  $i$  and  $j$ , we compute the Euclidean distance  $d_{ij} = \|\mathbf{x}_i - \mathbf{x}_j\|$  and the unsigned angle between their polarity vectors  $\theta_{ij} = \arccos(\mathbf{p}_i \cdot \mathbf{p}_j)$ , which is rotation invariant. These quantities, together with gene expression vectors, are concatenated to form the edge feature,

$$\mathbf{e}_{ij} = [\mathbf{g}_i \|\mathbf{g}_j\| d_{ij} \|\theta_{ij}] \quad (1)$$

which is rotation invariant. From these edge features  $\mathbf{e}_{ij}$ , we compute pairwise messages  $\mathbf{m}_{ij} = \phi_e(\mathbf{e}_{ij})$  and attention weights  $\alpha_{ij} = \text{softmax}_j[\phi_\alpha(\mathbf{e}_{ij})]$ . In addition, we predict an equilibrium length  $\ell_{ij} = \phi_\ell(\mathbf{g}_i, \mathbf{g}_j)$ , which sets a preferred separation between agents  $i$  and  $j$ , analogous to the minimum of a harmonic potential of the form  $(d_{ij} - \ell_{ij})^2$ . These quantities are then aggregated to compute the forces that govern how each agent's position and internal states change over time as follows,

$$\begin{aligned} \dot{\mathbf{x}}_i &= \mathbf{f}_i^{\mathbf{x}} = \sum_{j \neq i} \alpha_{ij} \left( 1 - \frac{\ell_{ij}}{d_{ij}} \right) (\mathbf{x}_i - \mathbf{x}_j) \phi_{\mathbf{x}}(\mathbf{m}_{ij}) + \sigma_{\mathbf{x}} \boldsymbol{\xi}_i^{\mathbf{x}} \\ \dot{\mathbf{g}}_i &= \mathbf{f}_i^{\mathbf{g}} = \phi_{\mathbf{g}}(\mathbf{g}_i \|\mathbf{m}_i) + \sigma_{\mathbf{g}} \boldsymbol{\xi}_i^{\mathbf{g}} \quad \text{where} \quad \mathbf{m}_i = \sum_{j \neq i} \alpha_{ij} \mathbf{m}_{ij} \\ \dot{\mathbf{p}}_i &= \mathbf{f}_i^{\mathbf{p}} = \phi_{\mathbf{p}}(\mathbf{g}_i \|\mathbf{m}_i) + \sigma_{\mathbf{p}} \boldsymbol{\xi}_i^{\mathbf{p}} \end{aligned} \quad (2)$$

where the dot notation denotes the time derivative,  $\sigma(\cdot)$  the noise strengths, and  $\boldsymbol{\xi}^{(\cdot)}$  are the corresponding Gaussian white noises. Supplementary Information section 8 provides the pseudocode for the force computation procedure.

#### *Numerical integration*

The position and internal states of each agent are updated with the corresponding forces in equation (2) using a Neural SDE solver [37–39], enabling end-to-end differentiable morphogenesis simulation. The numerical integration to a fixed final time  $T$  yields the trajectories  $\{\mathbf{X}^t, \mathbf{G}^t, \mathbf{P}^t\}_{t=0}^T$ . With this differentiability, the force model's MLP parameters  $\mathbf{w}$  are learned using gradients of the shape-matching loss,  $\nabla_{\mathbf{w}} \mathcal{L}_{\text{s.m.}}(\mathbf{w}; \{\mathbf{X}^0, \mathbf{G}^0, \mathbf{P}^0\})$ , via the ADAM

optimizer [68]. The full set of model hyperparameters and integration parameters used in the DiffeoMorph experiments is provided in the subsequent ‘Details of experimental setup’ section.

### Shape-matching loss

#### Spectral representation of 3D shapes

Consider a point cloud representing the positions of  $N$  agents evolved by an agent-based model, denoted by  $\mathbf{X}^{\text{evol}} \in \mathbb{R}^{N \times 3}$  and expressed in a chosen Cartesian laboratory frame. Our goal is to compare it with a target shape represented by  $\mathbf{X}^{\text{target}} \in \mathbb{R}^{M \times 3}$  where  $M$  may differ from  $N$  and, even when it does not, the point-to-point correspondence between two shapes may not be known. To perform shape comparison in permutation-invariant and agent-number-agnostic manner, we seek to treat these matrices as discrete approximations of functions over space and expand them in suitable basis functions.

To this end, we first constrain  $\mathbf{X}^{\text{evol}}$  to lie within the unit ball  $B_1(0)$  as  $\mathbf{X}_B^{\text{evol}} = (\mathbf{X}^{\text{evol}} - \mathbf{X}_{\text{c.o.m}}^{\text{evol}})/r_{\max}$  where  $\mathbf{X}_{\text{c.o.m}}^{\text{evol}}$  denotes the center-of-mass coordinates broadcasted over all rows of  $\mathbf{X}^{\text{evol}}$  and  $r_{\max}$  is the largest radius of the centered target point cloud. For clarity, we omit the superscript in what follows. We define the following normalized empirical measure supported in the unit ball  $B_1(0)$ :

$$\mu(\mathbf{x}) = \frac{1}{N} \sum_{i=1}^N \omega_i \delta(\mathbf{x} - \mathbf{x}_{B,i}), \quad (3)$$

where we allow each point to be associated with a distinct learnable weight  $\omega_i$ . We expand  $\mu$  in real 3D Zernike polynomials  $Z_{n\ell m}$ —which form an orthonormal basis of  $L^2(B_1(0))$ —with truncation parameters  $n_{\max}$  and  $\ell_{\max}$  as,

$$\mu(\mathbf{x}) = \sum_{n=0}^{n_{\max}} \sum_{\ell=0}^{\ell_{\max}} \sum_{m=-\ell}^{\ell} c_{n\ell m} \underbrace{R_{n\ell}(r)}_{Z_{n\ell m}(\mathbf{x})} \underbrace{Y_{\ell m}^{\text{real}}(\theta, \phi)}_{\text{radial angular}} \quad (4)$$

$$\text{where } c_{n\ell m} = \langle \mu, Z_{n\ell m} \rangle = \frac{1}{N} \sum_{i=1}^N \omega_i R_{n\ell}(r_i) Y_{\ell m}(\theta_i, \phi_i) \quad (5)$$

In this functional representation, the 3D shape of simulation is registered via the coefficients of the 3D Zernike polynomials, or Zernike moments,  $\mathbf{C} := \{c_{n\ell m}\}$ , obtained from the projection in equation (5). These can be viewed as a spectrum that contains both radial and angular variation of the shape. The mathematical properties of the 3D Zernike polynomials are discussed in Supplementary Information section 1.

The summation over all agent  $i$  in the projection, the normalization in the definition of the empirical measure, and the subtraction of the center-of-mass position ensure invariance to agent index permutation, the total number of agents, and global translation, respectively.

#### Spectral alignment for rotation invariance

Zernike moments  $\mathbf{C}$  remain sensitive to orientation because the azimuthal index  $m$  of the spherical harmonics depends on the orientation of the shape with respect to the coordinate axes of the laboratory frame. Consequently, the Zernike moments of a rotated shape differ from those of the original.

Instead of collapsing the azimuthal indices  $m$ , either by computing the norm [27] or higher-order spectrum [69], which would compromise the discriminative power of spectral representation or require additional computations, respectively, we seek an alternative approach where we align spectra of two shapes before direct comparison in order to achieve rotation invariance. Given two Zernike moments  $\mathbf{C}$  and  $\tilde{\mathbf{C}}$  computed from two 3D shapes with different orientations but otherwise the same overall geometry, Wigner-D matrices  $D^\ell \in \mathbb{R}^{(2\ell+1) \times (2\ell+1)}$  at each angular degree  $\ell$  can rotate one into the other according to  $\tilde{c}_{n\ell m} = \sum_{m'} D_{mm'}^\ell c_{n\ell m'}$ , which holds for all radial order  $n$  as  $R_{n\ell}$  does not depend on rotation. They are parameterized by a unit quaternion  $\mathbf{q} = (q_w, q_x, q_y, q_z)$  as,

$$D_{m'm}^\ell(\mathbf{q}) = (Q^\ell)^\dagger \left[ \sqrt{\frac{(\ell+m)!(\ell-m)!}{(\ell+m')!(\ell-m')!}} \sum_{\rho} (-1)^\rho \binom{\ell+m'}{\rho} \binom{\ell-m'}{\ell-\rho-m} \mathbf{q}_a^{\ell+m'-\rho} \bar{\mathbf{q}}_a^{\ell-\rho-m} \mathbf{q}_b^{\rho-m'+m} \bar{\mathbf{q}}_b^{\rho} \right] Q^\ell \quad (6)$$

where  $\mathbf{q}_a = q_w + iq_z$  and  $\mathbf{q}_b = q_y + iq_x$  are the Cayley–Klein parameters,  $Q^\ell$  is the real-to-complex change-of-basis transformation for spherical harmonics of angular degree  $\ell$  (i.e.,  $Y_{\ell m}^{\text{complex}} = Q_{mm'}^\ell Y_{\ell m'}^{\text{real}}$ ), and  $\bar{z}$  denotes the complex conjugate of  $z$ .

Let  $\varphi_{\mathbf{w}}^T$  denotes the integration of our SE(3)-equivariant force model parameterized by weight  $\mathbf{w}$ , which evolves the the initial configuration  $\mathbf{X}^0$  over time  $T$  into the evolved configuration  $\mathbf{X}^{\text{evol}}$ , and  $\Phi$  the function that constrains a point cloud to the unit ball and project it onto the 3D Zernike polynomials—such that  $\mathbf{X}^{\text{evol}} = \varphi_{\mathbf{w}}^T(\mathbf{X}^0)$  and  $\mathbf{C}^{\text{evol}} = \Phi(\mathbf{X}^{\text{evol}})$ . We can formulate the desired shape-matching objective for learning morphogenesis parameters  $\mathbf{w}$  as the outer loss of the following bilevel optimization problem,

$$\mathcal{L}_{\text{s.m.}}(\mathbf{w}; \mathbf{X}^0) = \frac{1}{N_{\text{spec}}} \sum_{n=0}^{n_{\text{max}}} \sum_{\ell=0}^{\ell_{\text{max}}} \sum_{m, m'=-\ell}^{\ell} \left\| c_{n\ell m}^{\text{target}} - D_{mm'}^\ell(\mathbf{q}^*(\mathbf{w})) c_{n\ell m'}^{\text{evol}} \right\|^2 + \frac{\lambda}{N_{\text{agent}}} \|\mathbf{x}_{\text{c.o.m}}^{\text{evol}}\|^2 \quad (7)$$

where  $N_{\text{spec}}$  is the the total number of  $(n, \ell, m)$  spectral index configurations appearing in the expansion and  $\mathbf{x}_{\text{c.o.m}}^{\text{evol}}$  is the center-of-mass coordinates, and the optimal unit quaternion  $\mathbf{q}^*(\mathbf{w})$  for a given  $\mathbf{w}$  is found in the inner optimization,

$$\begin{aligned} \mathbf{q}^*(\mathbf{w}) &= \arg \max_{\mathbf{q}} \mathcal{M}(\mathbf{q}; \mathbf{w}) \\ \text{where } \mathcal{M}(\mathbf{q}; \mathbf{w}) &= \frac{1}{N_{\text{spec}}} \sum_{n=0}^{n_{\text{max}}} \sum_{\ell=0}^{\ell_{\text{max}}} \sum_{m, m'=-\ell}^{\ell} c_{n\ell m}^{\text{target}} D_{mm'}^\ell(\mathbf{q}) c_{n\ell m'}^{\text{evol}} \end{aligned} \quad (8)$$

which we refer to as the spectral overlap as it maximizes the alignment between the rotated and the target spectra, and solve using gradient updates as there is no closed-form solution. The spectral overlap  $\mathcal{M}$  corresponds to the cross term of spectral MSE of  $\mathcal{L}_{\text{s.m.}}$  because  $D^\ell(\mathbf{q})^\top D^\ell(\mathbf{q}) = \mathbf{I}$ , owing to the orthogonality of  $D^\ell$ . With all  $m$  components retained, the shape matching can distinguish chirality while remaining rotation invariant.

The second term in the outer loss—a center-of-mass correction—prevents the force model from exploiting a trivial global-drift strategy. Without this constraint, the model could generate the crescent shape by moving the entire point cloud in one direction while assigning slightly different velocities across it—one tip moving faster, the other slower, with the intermediate points following at adjusted speeds and angles. This would produce an apparent curvature through coordinated drift rather than through actual shape deformation.

Because a valid rotation is represented by a unit quaternion, the optimization must remain on the three-dimensional unit sphere  $S^3 \subset \mathbb{R}^4$ . Differentiating the spectral overlap  $\mathcal{M}$  with respect to the unit quaternion  $\mathbf{q}$  using automatic differentiation produces the usual Euclidean gradient  $\nabla_{\mathbf{q}} \mathcal{M} \in \mathbb{R}^4$ , which does not, in general, lie in the tangent space  $T_{\mathbf{q}} S^3$  of the unit sphere at  $\mathbf{q}$ . To obtain a gradient direction that respects the unit-norm constraint, we project the Euclidean gradient onto the tangent space at  $\mathbf{q}$ , yielding the Riemannian gradient

$$\nabla_{\mathbf{q}}^{S^3} \mathcal{M} = (\mathbf{I} - \mathbf{q} \mathbf{q}^\top) \nabla_{\mathbf{q}} \mathcal{M}, \quad (9)$$

where  $\mathbf{I} - \mathbf{q} \mathbf{q}^\top$  is the orthogonal projector onto the tangent space of the sphere at  $\mathbf{q}$ .

We update the unit quaternion with ADAM optimizer along the geodesic of this tangent vector using the exponential map:

$$\mathbf{q}_{k+1} = \text{Exp}_{\mathbf{q}_k}(-\eta v) := \cos(\eta \|v\|) \mathbf{q}_k - \sin(\eta \|v\|) \frac{v}{\|v\|} \quad (10)$$

where  $\eta$  is the step size and  $v = \nabla_{\mathbf{q}}^{S^3} \mathcal{M}$ . These steps ensure that  $\mathbf{q}$  remains on the unit sphere after each gradient update and thus continues to represent a valid rotation throughout optimization.

#### Implicit differentiation of alignment optimization

Minimizing the outer loss of equation (7) requires computing the Jacobian  $\nabla_{\mathbf{w}} \mathbf{q}^*$ . Taking advantage of the structure of the unit quaternion optimization problem, we propose to compute this Jacobian using implicit differentiation as follows,

$$\nabla_{\mathbf{w}} \mathbf{q}^* = -[\mathbf{P} (\nabla_{\mathbf{q}\mathbf{q}}^2 \mathcal{M} - \alpha \mathbf{I}) \mathbf{P}]^{-1} \nabla_{\mathbf{w}, \mathbf{q}}^2 \mathcal{M} \quad (11)$$

where  $\mathbf{P} = \mathbf{I} - \mathbf{q} \mathbf{q}^\top$ ,  $\nabla_{\mathbf{w}, \mathbf{q}}^2 = \nabla_{\mathbf{w}} \circ \nabla_{\mathbf{q}}^{S^3}$ , and  $\alpha = \mathbf{q}^\top \nabla_{\mathbf{q}} \mathcal{M}$ . Note that  $\nabla_{\mathbf{q}\mathbf{q}}^2$  is the Euclidean Hessian in  $\mathbb{R}^4$ , while the term inside the square brackets is its Riemannian counterpart on  $T_{\mathbf{q}} S^3$ .

The expression requires inverting the Hessian, an inevitable trade-off when employing implicit differentiation. However, since the optimization parameters are just the four components of a unit quaternion, inverting the resulting  $4 \times 4$  matrix is computationally trivial. Note that the Hessian is  $4 \times 4$  because we retain the radial zero mode along the direction of  $\mathbf{q}$ . We prove in Supplementary Information Section 3 that the Riemannian Hessian in the intrinsic three-dimensional coordinates is invertible as long as  $\mathbf{X}^{\text{evol}}$  does not have continuous rotational symmetry. During training, we invert the  $4 \times 4$  Hessian via the Moore–Penrose Pseudoinverse, which removes the radial zero mode. In practice, the discrete nature of a point cloud, the slight elongation of the initial shape, stochastic noise introduced during simulation, and the use of pseudo-inverse together ensure robust optimization. The derivation of the Riemannian Hessian, its behavior under rotational symmetry, and the comparison between unit quaternion parameterization and the more common Euler angle parameterization are provided in Supplementary Information sections 4, 5, and 6, respectively.

#### Implementation details

*a. Projection.* We precomputed the expressions of the radial polynomials  $R_{nl}$  up to  $n_{\max}=20$  and  $\ell_{\max}=10$  to avoid repeatedly calculating terms for the Jacobi and the associated Legendre polynomials. We use `e3nn` library [70] to compute spherical harmonics  $Y_{\ell m}$ . We use `vmap` function to vectorize the projection over each  $n$ ,  $\ell$ , and  $m$  in equation (5). Since the shape of tensors passed to `vmap` should be identical, for each  $\ell$ -row of  $Y_{\ell m}$ , we assign the expression of the  $m$ -th real spherical harmonics starting from the first column and zero-padded the azimuthal  $m$  indices after  $2\ell+1$  up to  $2\ell_{\max}+1$ .  $Y_{\ell m}$  is thus a matrix of size  $10 \times 21$ . Regarding radial polynomials,  $n$  and  $\ell$  of  $R_{nl}$  should satisfy:  $n-\ell$  must be even and  $n > \ell$ . We chose  $n_{\max}=20$  and, for each  $\ell$ , assigned the expression of nonzero  $n$ -th radial polynomial starting from the first column.  $R_{nl}$  is a matrix of size  $20 \times 10$ .

*b. Spectral Rotation.* We precomputed binomial terms and the factorial-based prefactor term in the Wigner–D matrix expression in equation (6) for all  $(\ell, m, m', \rho)$  configurations up to  $\ell_{\max}=10$ , and use these values as lookup tables when computing the Wigner–D matrix. We vectorize the computation over  $(m, m', \rho)$  at each  $\ell$ . Vectorizing over  $\ell$  would yield further speedup, but requires additional memory for zero-padding. We did not implement it because the loss runtime is already small compared to other metrics benchmarked in Fig. 3d.

#### Preparation of initial states

In DiffeoMorph, we learn a distributed morphogenesis control protocol based on the evolving states of individual agents. To make the learning problem biologically realistic and algorithmically nontrivial, we initialize the positions, gene expression profiles, and polarity of agents in a way that provides only minimal spatial cues so that effective morphogenesis requires inter-agent communication. All polarity vectors  $\mathbf{p}_i^0$  are aligned along the same random direction, and the initial positions and gene expression profiles are defined as follows.

#### Positions

Since most morphogenesis processes in developmental biology originate from a nearly spherical aggregate of cells, we prepare  $\mathbf{X}^0$  as a sphere-shaped point cloud consisting of a shell and a core. The shell is generated using the Fibonacci lattice [42], which provides a quasi-uniform discretization over  $S^2$  with locally isotropic neighborhoods that appear visually uniform. The core is filled using Poisson-disk sampling [43], which produces a random yet evenly spaced distribution of points by enforcing a minimum separation distance—note that no algorithm can generate a perfectly uniform grid in the unit ball. Together, these constructions yield an approximately uniform initial point cloud. The point cloud is then elongated by 10% along a body axis (see the next section to see how this is chosen) to break spherical symmetry so that the rotational eigenvalues of the Riemannian Hessian in equation (11) are no longer all near zero. Additionally, we perturb the point cloud at every training step by adding zero-mean Gaussian noise with a prescribed noise magnitude—0.05 for the ellipsoid and crescent experiments and 0.03 for the bunny experiment—to ensure robust implicit differentiation and encourage the force model to learn a generalizable morphogenesis protocol.

#### Gene expression profiles

Taking inspiration again from developmental biology, we interpret the elongation as originating from a preceding, localized morphogen expression at a pole, which establishes the elongation axis and thereby sets the body axis [58].

To encode this spatial cue on the point cloud, we randomly sample a unit vector as body axis, project all cells onto this vector, and identify the cell with the maximal projection—this marks the pole. We then select its  $N_{\text{org}}-1$  nearest neighbors on the shell to define  $N_{\text{org}}$  “organizer cells” expressing the morphogens. These cells are assigned the one-hot gene expression  $\mathbf{g}_i=[1, 0, \dots, 0]$ , while all remaining cells are assigned  $\mathbf{g}_i=[0, \dots, 0, 1]$ . The point cloud is then elongated along the sampled direction.

When introducing additional groups of organizer cells, we sample new unit vectors that are  $90^\circ$  apart from the previously chosen pole axis (with the third axis determined by the right-hand rule), and again select  $N_{\text{org}}$  organizer cells around each new pole. The second group receives  $\mathbf{g}_i=[0, 1, 0, \dots, 0]$ , and the third receives  $\mathbf{g}_i=[0, 0, 1, 0, \dots, 0]$ . These assignments encode morphogen signals that define left-right and front-back symmetry axes. In contrast to the primary body axis, no perturbation is applied along these additional directions.

### Details of experimental setup

#### Spectral Shape Alignment

To generate point clouds used in Fig. 2b,c, we downloaded the point cloud format of the Stanford Bunny from the Stanford 3D Scanning Repository. We shifted the point cloud with  $N=2503$  points and scaled it to the unit ball by dividing the coordinates of the points by the maximum of the radial distance. To generate the crescent-shaped point cloud, we sampled  $N=5000$  points uniformly within the unit ball. Next, we elongated the points along the  $z$ -axis by a factor of 3, and bent the resulting ellipsoid into a crescent shape by using the following arc transformation for each point  $i$ ,

$$\begin{aligned} \text{Bending angle : } & \theta_i = y_i/R \\ \text{New } x\text{-coordinate : } & x_i^{\text{new}} = R(1 - \cos \theta_i) + x_i \\ \text{New } z\text{-coordinate : } & z_i^{\text{new}} = R \sin(\theta_i) \end{aligned}$$

Finally, we assigned a weight value of 1 to a point where  $z_i \geq 0$  and a weight value of 2 to a point where  $z_i < 0$ . We used orange and blue colors to represent the weight values of 1 and 2, respectively.

For optimization, we set  $\ell_{\text{max}}=8$  and initialized a unit quaternion along a random direction. We iterated the gradient ascent steps with a learning rate  $\eta=5\text{e-}3$  and terminated the training when the spectral overlap  $\mathcal{M}$  changed by less than the threshold value of  $1\text{e-}8$ .

#### Direct Shape Optimization

For the analysis shown in Fig. 2d,e, we generated a target crescent-shaped point cloud with  $N=3000$  points by following the procedure described above, elongating along the  $y$ -axis by a factor of 3 and applying the arc transformation based on the  $z$  coordinates. We did not normalize the point cloud. We generated two ellipsoid-shaped clouds of sizes  $N=3000$  and  $N=1000$ , both with an elongation factor of 2, and then rotated them to the orientations shown in Fig. 2d. We used the original coordinates of the point cloud format of the Stanford Bunny from Stanford 3D Scanning Repository and assign a weight  $\omega_i=1$  if  $z_i \geq 2.75$  and 2 otherwise. The initial point clouds, with sizes  $N=2000$  and  $N=800$ , were prepared as described above. All points were initialized with the weight value of 1. We used the same color scheme for the weight visualization as above.

We normalized an evolved point cloud by  $r_{\text{max}}$  of the respective target structure to obtain the correct absolute scaling. We used  $\ell_{\text{max}}=10$  and again initialized a unit quaternion along a random direction. For the inner optimization, we optimized the unit quaternion with a learning rate  $\eta_{\text{inner}}=1\text{e-}1$  and a threshold  $\delta_{\text{inner}}=1\text{e-}8$ . For the outer optimization, we learned the coordinates  $\mathbf{X}$  of points (and their weights  $\omega$  in the bunny experiment) with learning rates  $\eta_{\mathbf{X}}$  and  $\eta_{\omega}$  both set to  $5\text{e-}2$ . We terminated the training when the shape-matching loss  $\mathcal{L}_{\text{s.m.}}$  fell below  $\delta_{\text{outer}}=5\text{e-}5$ .

#### DiffeoMorph Experiments

In the experiments shown in Fig. 4, we generated the initial sphere-shaped point cloud consisting of a shell and a core as follows. We first constructed the unit-radius shell using a Fibonacci lattice of 250 agents, which produced a mean pairwise distance  $\langle r_{ij} \rangle=0.21$  with minimal variation across pairs. To obtain a core whose inter-agent spacing is comparable to  $\langle r_{ij} \rangle$ , we sample points inside a sphere of radius  $1-\langle r_{ij} \rangle$  using Poisson-disk sampling with minimum

separation distance set to  $\langle r_{ij} \rangle$ , which resulted in 175 agents. Combining the shell and core samples produced a point cloud that approximates a uniform distribution of points over the unit ball. We verified that DiffeoMorph training is robust to different agent counts. For all experiments reported in Fig. 4, we used this point cloud with  $N_{\text{agent}}=425$ , which provides sufficient resolution for clear visualization of shapes while keeping training times reasonable: approximately 5 minutes, 20 minutes, and 90 minutes for the ellipsoid, crescent, and bunny experiments, respectively, on an NVIDIA RTX 6000 Ada Generation GPU. We constructed the target ellipsoid and crescent shapes as described above. As for the bunny, we subsampled the original Stanford Bunny coordinates from VolGallery repository to 10000 points and scaled it up so that  $r_{\text{max}}=3.5$ . This yields a point cloud representing a volumetric bunny shape, in contrast to the previously described, shell-only bunny point cloud.

For all three structures, we set the dimensionality of the gene expression vector  $\mathbf{g}$  to 32. All MLPs in the force model were set to have three hidden layers with 32 units. We used **SiLU** [71] (or **Swish**) activation function to obtain a smooth, numerically stable vector field. For numerical integration, we used **Euler** solver of the **Diffraex** library [39] with timestep  $\text{dt}=0.01$ . We modified the solver to renormalize the updated polarity vectors to unit norm vector after each update. For training, we used  $\eta_{\text{inner}}=1\text{e-}2$ ,  $\delta_{\text{inner}}=1\text{e-}7$  for the spectral alignment (inner optimization) and set  $\eta_{\text{outer}}$  to  $2\text{e-}3$ ,  $1\text{e-}3$ , and  $5\text{e-}3$  for the force model training (outer optimization) in the ellipsoid, crescent, and bunny experiments, respectively. We early stopped the force model training when loss did not improve for 150 steps for the ellipsoid and crescent experiments, and for 250 steps for the bunny experiment. We again normalized an evolved point cloud by  $r_{\text{max}}$  of the respective target structure. We used  $N_{\text{org}}=10$  for the ellipsoid and crescent experiments and  $N_{\text{org}}=20$  for the bunny experiment. During evolution, we added Brownian noise of magnitude  $\sigma_{\mathbf{x}/\mathbf{p}}=0.002$  to the positions and polarity vectors to introduce stochasticity into morphogenesis dynamics. We set  $\sigma_{\mathbf{g}}=0$  to make the gene expression dynamics deterministic.

The MSE loss for the generalization under organizer shifts shown in Fig. 4c was evaluated by performing a fresh spectral alignment optimization for each test sample. For the ellipsoid and crescent experiments, we warm-started this optimization using the optimal unit quaternion  $\mathbf{q}^*$  obtained during training. In the bunny experiment, however, we observed that initializing with  $\mathbf{q}^*$  sometimes resulted in a high test loss—even when the evolved shape visually reproduces the bunny—suggesting that the alignment optimization, starting from the training orientation, became trapped in a local maximum due to the high-frequency modes of the bunny morphology. To address this, we reorient  $\mathbf{q}^*$  by first computing the quaternion  $\mathbf{q}_{1 \rightarrow 0}$  that reverses the organizer shift—from the shifted direction  $\mathbf{u}_1$  back to the original direction  $\mathbf{u}_0$ , which define the regions of the red organizer cells in Fig. 4a,b)—as follows:

$$\mathbf{q}_{1 \rightarrow 0} = \left( \cos \frac{\theta}{2}, \mathbf{v} \sin \frac{\theta}{2} \right) \quad \text{where} \quad \theta = \arccos(\mathbf{u}_1 \cdot \mathbf{u}_0) \quad \text{and} \quad \mathbf{v} = \frac{\mathbf{u}_1 \times \mathbf{u}_0}{\|\mathbf{u}_1 \times \mathbf{u}_0\|}$$

and then updated the unit quaternion used for the loss evaluation to  $\mathbf{q}_{\text{new}} = \mathbf{q}^* \otimes \mathbf{q}_{1 \rightarrow 0}$  where  $\otimes$  denotes quaternion multiplication. This procedure yielded test loss values slightly higher than those obtained under noise addition, as summarized in Fig. 4c.

For the trajectory analysis in Fig. 5, we standardized the gene expression values across all time snapshots and computed two-dimensional UMAP coordinates using the implementation of McInnes *et al.* [72] with  $n_{\text{neighbors}}=200$  and  $\text{min\_dist}=0.1$ . We found that the resulting UMAP embedding showed only small variation when modifying  $n_{\text{neighbors}}$  in the range 50–400 and  $\text{min\_dist}$  in the range 0.1–1. Clusters in Fig. 5b were found using the Leiden algorithm [73] as implemented in the **Scanpy** library [74] with 30-nearest-neighbor graph constructed from the final-time UMAP coordinates, with the cluster resolution parameter set to 0.02. The same UMAP and clustering parameters were used for all three experiments.

## DATA AVAILABILITY

The surface point cloud of Stanford Bunny is available at <http://graphics.stanford.edu/data/3Dscanrep>. The volumetric point cloud of Stanford Bunny is available via GitHub at <https://github.com/dcoeurjo/VolGallery>. The processed point clouds used in experiments are available via GitHub at <https://github.com/hormoz-lab/diffeomorph>.

## CODE AVAILABILITY

The source code of DiffeoMorph is available via GitHub at <https://github.com/hormoz-lab/diffeomorph>.

## ACKNOWLEDGMENTS

We thank Christoph Budjan for helpful discussions. This work was supported by the National Heart, Lung, and Blood Institute (NHLBI) of the National Institutes of Health (NIH) under award R01HL158269, and by the Barry Family HSCI Innovation Award for Early Investigators from the Harvard Stem Cell Institute (HSCI).

---

[1] S. F. Gilbert and M. J. F. Barresi, *Developmental Biology*, 12th ed. (Sinauer Associates, Oxford University Press, New York, NY, 2020).

[2] P. Hogeweg, Evolving mechanisms of morphogenesis: on the interplay between differential adhesion and cell differentiation, *Journal of Theoretical Biology* **203**, 317 (2000).

[3] B. P. Teague, P. Guye, and R. Weiss, Synthetic morphogenesis, *Cold Spring Harbor perspectives in biology* **8**, a023929 (2016).

[4] M. Takeichi, Dynamic contacts: rearranging adherens junctions to drive epithelial remodelling, *Nature reviews Molecular cell biology* **15**, 397 (2014).

[5] J. B. Gurdon and P.-Y. Bourillot, Morphogen gradient interpretation, *Nature* **413**, 797 (2001).

[6] G. M. Whitesides and B. Grzybowski, Self-assembly at all scales, *Science* **295**, 2418 (2002).

[7] K. A. Athanasiou, R. Eswaramoorthy, P. Hadidi, and J. C. Hu, Self-organization and the self-assembling process in tissue engineering, *Annual review of biomedical engineering* **15**, 115 (2013).

[8] S. C. Goldstein, J. D. Campbell, and T. C. Mowry, Programmable matter, *Computer* **38**, 99 (2005).

[9] M. Rubenstein, A. Cornejo, and R. Nagpal, Programmable self-assembly in a thousand-robot swarm, *Science* **345**, 795 (2014).

[10] A. Fatehullah, S. H. Tan, and N. Barker, Organoids as an in vitro model of human development and disease, *Nature cell biology* **18**, 246 (2016).

[11] H. Clevers, Modeling development and disease with organoids, *Cell* **165**, 1586 (2016).

[12] R. S. Sutton, A. G. Barto, *et al.*, *Reinforcement learning: An introduction*, Vol. 1 (MIT press Cambridge, 1998).

[13] R. Lowe, Y. I. Wu, A. Tamar, J. Harb, O. Pieter Abbeel, and I. Mordatch, Multi-agent actor-critic for mixed cooperative-competitive environments, *Advances in neural information processing systems* **30** (2017).

[14] B. Baker, I. Kanitscheider, T. Markov, Y. Wu, G. Powell, B. McGrew, and I. Mordatch, Emergent tool use from multi-agent autocurricula, in *International Conference on Learning Representations (ICLR)* (2020).

[15] D. Pathak, C. Lu, T. Darrell, P. Isola, and A. A. Efros, Learning to control self-assembling morphologies: a study of generalization via modularity, *Advances in Neural Information Processing Systems* **32** (2019).

[16] C. Lin, T. Fan, W. Wang, and M. Nießner, Modeling 3d shapes by reinforcement learning, in *Computer Vision–ECCV 2020: 16th European Conference, Glasgow, UK, August 23–28, 2020, Proceedings, Part X 16* (Springer, 2020) pp. 545–561.

[17] J. Viquerat, J. Rabault, A. Kuhnle, H. Ghraieb, A. Larcher, and E. Hachem, Direct shape optimization through deep reinforcement learning, *Journal of Computational Physics* **428**, 110080 (2021).

[18] R. Deshpande, F. Mottes, A.-D. Vlad, M. P. Brenner, and A. Dal Co, Engineering morphogenesis of cell clusters with differentiable programming, *Nature Computational Science* **5**, 875 (2025).

[19] A. Mordvintsev, E. Randazzo, E. Niklasson, and M. Levin, Growing neural cellular automata, *Distill* **5**, e23 (2020).

[20] R. B. Palm, M. González-Duque, S. Sudhakaran, and S. Risi, Variational neural cellular automata, in *Proceedings of the 10th International Conference on Learning Representations (ICLR)* (2022).

[21] D. Zhang, C. Choi, J. Kim, and Y. M. Kim, Learning to generate 3d shapes with generative cellular automata, in *Proceedings of the International Conference on Learning Representations (ICLR)* (2021).

[22] D. Grattarola, L. Livi, and C. Alippi, Learning graph cellular automata, in *Advances in Neural Information Processing Systems*, Vol. 34 (2021) pp. 20983–20994.

[23] M. Tesfaldet, D. Nowrouzezahrai, and C. Pal, Attention-based neural cellular automata, in *Advances in Neural Information Processing Systems*, Vol. 35 (Curran Associates, Inc., 2022) pp. 8174–8186.

[24] K. Niu and C. Tian, Zernike polynomials and their applications, *Journal of Optics* **24**, 123001 (2022).

[25] M. Novotni and R. Klein, Shape retrieval using 3d zernike descriptors, *Computer-Aided Design* **36**, 1047 (2004).

[26] M. Kazhdan, T. Funkhouser, and S. Rusinkiewicz, Rotation invariant spherical harmonic representation of 3 d shape descriptors, in *Symposium on geometry processing*, Vol. 6 (2003) pp. 156–164.

[27] M. Novotni and R. Klein, 3d zernike descriptors for content based shape retrieval, in *Proceedings of the eighth ACM symposium on Solid modeling and applications* (2003) pp. 216–225.

[28] R. Scoccimarro, The bispectrum: from theory to observations, *The Astrophysical Journal* **544**, 597 (2000).

[29] R. Kakarala, The bispectrum as a source of phase-sensitive invariants for fourier descriptors: a group-theoretic approach, *Journal of Mathematical Imaging and Vision* **44**, 341 (2012).

[30] W. Collis, P. White, and J. Hammond, Higher-order spectra: the bispectrum and trispectrum, *Mechanical systems and signal processing* **12**, 375 (1998).

[31] H. Fan, H. Su, and L. J. Guibas, A point set generation network for 3d object reconstruction from a single image, in *Proceedings of the IEEE conference on computer vision and pattern recognition* (2017) pp. 605–613.

- [32] Y. Rubner, C. Tomasi, and L. J. Guibas, The earth mover's distance as a metric for image retrieval, *International journal of computer vision* **40**, 99 (2000).
- [33] G. Gala, D. Grattarola, and E. Quaeghebeur, E (n)-equivariant graph neural cellular automata, *Transactions on Machine Learning Research* **2024** (2024).
- [34] F. Mémoli, Gromov–wasserstein distances and the metric approach to object matching, *Foundations of computational mathematics* **11**, 417 (2011).
- [35] V. G. Satorras, E. Hoogeboom, and M. Welling, E (n) equivariant graph neural networks, in *International conference on machine learning* (PMLR, 2021) pp. 9323–9332.
- [36] A. Vaswani, N. Shazeer, N. Parmar, J. Uszkoreit, L. Jones, A. N. Gomez, L. Kaiser, and I. Polosukhin, Attention is all you need, *Advances in neural information processing systems* **30** (2017).
- [37] R. T. Chen, Y. Rubanova, J. Bettencourt, and D. K. Duvenaud, Neural ordinary differential equations, *Advances in neural information processing systems* **31** (2018).
- [38] B. Tzen and M. Raginsky, Neural stochastic differential equations: Deep latent gaussian models in the diffusion limit, *arXiv preprint arXiv:1905.09883* (2019).
- [39] P. Kidger, *On Neural Differential Equations*, Ph.D. thesis, University of Oxford (2021).
- [40] M. Cuturi, Sinkhorn distances: Lightspeed computation of optimal transport, *Advances in neural information processing systems* **26** (2013).
- [41] G. Peyré, M. Cuturi, *et al.*, Computational optimal transport: With applications to data science, *Foundations and Trends® in Machine Learning* **11**, 355 (2019).
- [42] Á. González, Measurement of areas on a sphere using fibonacci and latitude–longitude lattices, *Mathematical Geosciences* **42**, 49 (2010).
- [43] R. Bridson, Fast poisson disk sampling in arbitrary dimensions, in *ACM SIGGRAPH 2007 sketches* (ACM, 2007) p. 22.
- [44] O. Wartlick, A. Kicheva, and M. González-Gaitán, Morphogen gradient formation, *Cold Spring Harbor perspectives in biology* **1**, a001255 (2009).
- [45] J. Briscoe and S. Small, Morphogen rules: design principles of gradient-mediated embryo patterning, *Development* **142**, 3996 (2015).
- [46] R. Harland and J. Gerhart, Formation and function of spemann's organizer, *Annual review of cell and developmental biology* **13**, 611 (1997).
- [47] E. M. De Robertis, Spemann's organizer and self-regulation in amphibian embryos, *Nature reviews Molecular cell biology* **7**, 296 (2006).
- [48] J. Jaeger, The gap gene network, *Cellular and Molecular Life Sciences* **68**, 243 (2011).
- [49] A. F. Schier, Nodal morphogens, *Cold Spring Harbor perspectives in biology* **1**, a003459 (2009).
- [50] E. M. De Robertis and H. Kuroda, Dorsal-ventral patterning and neural induction in xenopus embryos, *Annu. Rev. Cell Dev. Biol.* **20**, 285 (2004).
- [51] E. Becht, L. McInnes, J. Healy, C.-A. Dutertre, I. W. Kwok, L. G. Ng, F. Ginhoux, and E. W. Newell, Dimensionality reduction for visualizing single-cell data using umap, *Nature biotechnology* **37**, 38 (2019).
- [52] U. Alon, *An introduction to systems biology: design principles of biological circuits* (Chapman and Hall/CRC, 2019).
- [53] E. H. Davidson and M. S. Levine, Properties of developmental gene regulatory networks, *Proceedings of the National Academy of Sciences* **105**, 20063 (2008).
- [54] M. Murrell, P. W. Oakes, M. Lenz, and M. L. Gardel, Forcing cells into shape: the mechanics of actomyosin contractility, *Nature reviews Molecular cell biology* **16**, 486 (2015).
- [55] B. M. Gumbiner, Regulation of cadherin-mediated adhesion in morphogenesis, *Nature reviews Molecular cell biology* **6**, 622 (2005).
- [56] M. Levin, Endogenous bioelectrical networks store non-genetic patterning information during development and regeneration, *The Journal of physiology* **592**, 2295 (2014).
- [57] C. H. Waddington, *The strategy of the genes* (Routledge, 2014).
- [58] L. Wolpert, C. Tickle, and A. M. Arias, *Principles of development* (Oxford University Press, USA, 2015).
- [59] J. Delile, M. Herrmann, N. Peyriéras, and R. Doursat, A cell-based computational model of early embryogenesis coupling mechanical behaviour and gene regulation, *Nature communications* **8**, 13929 (2017).
- [60] C. M. Glen, M. L. Kemp, and E. O. Voit, Agent-based modeling of morphogenetic systems: Advantages and challenges, *PLoS computational biology* **15**, e1006577 (2019).
- [61] G. Guan, S. Wang, T. G. Shields, S. H. Pahng, C. X. Shao, J. Ye, C. Budjan, and S. Hormoz, Cooperative short-and long-range interactions enable robust symmetry breaking and axis formation, *bioRxiv* , 2025 (2025).
- [62] J. A. Sherratt and J. D. Murray, Models of epidermal wound healing, *Proceedings of the Royal Society of London. Series B: Biological Sciences* **241**, 29 (1990).
- [63] D. Lobo, W. S. Beane, and M. Levin, Modeling planarian regeneration: a primer for reverse-engineering the worm, *PLoS computational biology* **8**, e1002481 (2012).
- [64] J. S. Yodh, Y. Lin, S. Sinha, V. Krishnan, L. Mahadevan, and D. J. Cohen, Optimal bioelectric control accelerates collective wound healing, *bioRxiv* , 2025 (2025).
- [65] V. G. Kim, W. Li, N. J. Mitra, S. Chaudhuri, S. DiVerdi, and T. Funkhouser, Learning part-based templates from large collections of 3d shapes, *ACM Transactions on Graphics (TOG)* **32**, 1 (2013).
- [66] J. Gray and G. J. Hancock, The propulsion of sea-urchin spermatozoa, *Journal of Experimental Biology* **32**, 802 (1955).

- [67] A. J. Ijspeert, Central pattern generators for locomotion control in animals and robots: a review, *Neural networks* **21**, 642 (2008).
- [68] D. P. Kingma, Adam: A method for stochastic optimization, arXiv preprint arXiv:1412.6980 (2014).
- [69] W. Hu, Angular trispectrum of the cosmic microwave background, *Physical Review D* **64**, 083005 (2001).
- [70] M. Geiger and T. Smidt, e3nn: Euclidean neural networks, arXiv preprint arXiv:2207.09453 (2022).
- [71] P. Ramachandran, B. Zoph, and Q. V. Le, Searching for activation functions, arXiv preprint arXiv:1710.05941 (2017).
- [72] L. McInnes, J. Healy, N. Saul, and L. Grossberger, Umap: Uniform manifold approximation and projection, *The Journal of Open Source Software* **3**, 861 (2018).
- [73] V. A. Traag, L. Waltman, and N. J. Van Eck, From louvain to leiden: guaranteeing well-connected communities, *Scientific reports* **9**, 1 (2019).
- [74] F. A. Wolf, P. Angerer, and F. J. Theis, Scampy: large-scale single-cell gene expression data analysis, *Genome biology* **19**, 15 (2018).
- [75] B. C. Hall, Lie groups, lie algebras, and representations, in *Quantum Theory for Mathematicians* (Springer, 2013) pp. 333–366.
- [76] W. Fulton and J. Harris, *Representation theory: a first course*, Vol. 129 (Springer Science & Business Media, 2013).
- [77] K. Shoemake, Animating rotation with quaternion curves, in *Proceedings of the 12th annual conference on Computer graphics and interactive techniques* (1985) pp. 245–254.
- [78] J. You, Z. Ying, and J. Leskovec, Design space for graph neural networks, *Advances in Neural Information Processing Systems* **33**, 17009 (2020).

### Appendix 1: Mathematical Properties of 3D Zernike Polynomials

In this section, we briefly summarize the key properties of the 3D Zernike polynomials. For a complete discussion, we refer readers to Niu and Tian [24] and Novotni and Klein [25].

The 3D Zernike polynomials  $Z_{n\ell}^m(\mathbf{x})$ 's form a complete orthonormal basis of the Hilbert space  $L^2(B_1(0))$  and are constructed as the product of:

$$\text{Radial polynomial : } R_{n\ell}(r) = (-1)^n \sqrt{2} \sqrt{2n + \ell + \frac{1}{2} + 1} r^\ell P_n^{(\ell + \frac{1}{2}, 0)} (1 - 2r^2)$$

$$\text{Spherical harmonics : } Y_\ell^m(\theta, \phi) = (-1)^m \sqrt{\frac{2\ell + 1}{4\pi} \frac{\ell + |m|!}{(\ell + m)!}} P_\ell^{|m|}(\cos \theta) e^{im\phi}$$

where  $P_n^{(\alpha, \beta)}$  and  $P_l^m$  are the Jacobi and the associated Legendre polynomials and we used the orthonormal normalization scheme.

Any function  $f \in L^2(B_1(0))$  can be expanded in the 3D Zernike polynomial basis with coefficients given by the inner product,

$$c_{n\ell}^m = \langle f, Z_{n\ell}^m \rangle = \int_{\mathbb{B}^3} f(r, \theta, \phi) R_{n\ell}(r) \overline{Y_\ell^m(\theta, \phi)} r^2 \sin \theta dr d\theta d\phi \quad (\text{S1})$$

and, once truncated at suitable frequency cutoffs  $n_{\max}$  and  $\ell_{\max}$ ,  $c_{n\ell}^m$  give a compact representation of a function  $f$ .

Note that when a function  $f$  is real-valued, the complex-valued spherical harmonics  $Y_\ell^m$  can be converted to real-valued forms as,

$$Y_{\ell m}^{\text{real}} = \begin{cases} \frac{i}{\sqrt{2}} (Y_\ell^{-|m|} - (-1)^m Y_\ell^{|m|}) & \text{if } m < 0 \\ Y_\ell^0 & \text{if } m = 0 \\ \frac{1}{\sqrt{2}} (Y_\ell^{-|m|} + (-1)^m Y_\ell^{|m|}) & \text{if } m > 0 \end{cases} \quad (\text{S2})$$

This transformation rule defines the real-to-complex change-of-basis  $Q^\ell$ , whose entries satisfy

$$(Q^\ell)_{mm'} = \begin{cases} 1 & \text{if } m = 0 \text{ and } m' = 0 \\ -\frac{i}{\sqrt{2}} & \text{if } m < 0 \text{ and } m' = -|m| \\ \frac{1}{\sqrt{2}} & \text{if } m < 0 \text{ and } m' = |m| \\ \frac{i(-1)^{|m|}}{\sqrt{2}} & \text{if } m > 0 \text{ and } m' = -|m| \\ \frac{(-1)^{|m|}}{\sqrt{2}} & \text{if } m > 0 \text{ and } m' = |m| \\ 0 & \text{otherwise} \end{cases} \quad (\text{S3})$$

where  $m$  indexes the complex spherical harmonics and  $m'$  indexes the real spherical harmonics.

Using the real-valued form of the spherical harmonics ensures the resulting Zernike polynomials  $Z_{n\ell m}$  and their moments  $c_{n\ell m}$  are also real-valued. This real formulation is commonly adopted in machine learning applications, as most signals or functions of interest are real-valued, and deep learning libraries offer limited support for complex numbers.

In 'Shape-matching loss' section in the Methods, we model the scaled 3D point cloud by the empirical measure  $\mu(\mathbf{x}) = \frac{1}{N} \sum_{i=1}^N \omega_i \delta(\mathbf{x} - \mathbf{x}_i)$  and view it as an approximation of a continuous, square-integrable function  $f \in L^2(B_1(0))$ . We then proceed with the summation in equation (5) of the main text as the discrete analogue of the projection in equation (S1). Implicit in this operation is that we interpret the measure as a generalized function (i.e.,  $\mu \in \mathcal{D}'(B_1(0)) \neq L^2(B_1(0))$ ) that is dual to the test functions in  $\mathcal{D}(B_1(0))$ , which in our context are the 3D Zernike polynomials. Therefore, the moment computation in equation (5) is mathematically well-posed in the distributional sense. In practice, we can alternatively interpret equation (5) as a Monte-Carlo estimate of the continuous integral over the unit ball in equation (S1).

## Appendix 2: Constructing Representation of Lie Group SU(2) for Spectral Rotation

The spectral rotation matrix  $D_{\text{complex}}^\ell$  acts on the vector of complex spherical harmonics,

$$\mathbf{Y}_\ell = (Y_\ell^{-\ell}, Y_\ell^{-\ell+1}, \dots, Y_\ell^\ell)^\top,$$

which spans a  $(2\ell+1)$ -dimensional complex vector space. For each degree  $\ell$ , a rotation of this vector is represented by the unitary, irreducible  $(2\ell+1) \times (2\ell+1)$  matrix  $D^\ell$ , which is called the Wigner–D matrix. It is most often parameterized by Euler angles  $\boldsymbol{\xi} = (\alpha, \beta, \gamma)$  which specify successive rotations about the  $z$ ,  $y$ , and  $x$  axes, respectively in ZYX convention. It can also be parameterized by a unit quaternion  $\mathbf{q} = q_w + q_x \mathbf{i} + q_y \mathbf{j} + q_z \mathbf{k} = (q_w, q_x, q_y, q_z)$ . Below, we describe the procedure for constructing the Wigner–D matrix from both parameterizations. For further details, we refer interested readers to the standard references [75, 76].

### a. From Euler angles

For the Euler angle parameterization, we first need representations,  $J_x, J_y, J_z \in \mathbb{C}^{(2\ell+1) \times (2\ell+1)}$ , of the Lie algebra  $\mathfrak{su}(2)$ , which forms a basis of rotation about  $x$ ,  $y$ ,  $z$ -axis. To build them for each degree  $\ell$  with azimuthal indices  $m = -\ell, -\ell+1, \dots, \ell$ , we first define the “ladder” operators that shifts the index  $m$  by  $\pm 1$  as follows,

$$[J_+]_{mm'} = \sqrt{(\ell - m)(\ell + m + 1)} \delta_{m, m'+1} \quad [J_-]_{mm'} = \sqrt{(\ell + m)(\ell - m + 1)} \delta_{m, m'-1}$$

where  $\delta_{ij}$  denotes the Kronecker delta, and construct  $J_x$ ,  $J_y$ , and a diagonal  $J_z$  as,

$$J_x = \frac{1}{2}(J_+ + J_-) \quad J_y = \frac{1}{2i}(J_+ - J_-) \quad [J_z]_{m,m'} = m \delta_{m,m'}$$

Given these bases of rotation and the Euler angles  $(\alpha, \beta, \gamma)$ , we can build the irreducible representations of SU(2), in degree  $\ell$  basis, by computing the following matrix exponential,

$$R_z^\ell(\alpha) = \exp(-i\alpha J_z) \quad R_y^\ell(\beta) = \exp(-i\beta J_y) \quad R_x^\ell(\gamma) = \exp(-i\gamma J_x)$$

and the Wigner–D matrix as,

$$D_{\text{complex}}^\ell(\alpha, \beta, \gamma) = R_z^\ell(\alpha) R_y^\ell(\beta) R_x^\ell(\gamma) \quad (\text{S4})$$

### b. From a unit quaternion

For the unit quaternion parameterization, we can obtain one particular representation of SU(2) at  $\ell = 1/2$  directly via,

$$U(\mathbf{q}) = \begin{pmatrix} \mathbf{q}_a & \mathbf{q}_b \\ -\mathbf{q}_b^* & \mathbf{q}_a \end{pmatrix} \quad \text{where} \quad \mathbf{q}_a = q_w + \mathbf{i} q_z \quad \text{and} \quad \mathbf{q}_b = q_y + \mathbf{i} q_x \quad (\text{S5})$$

where  $\mathbf{q}_a$  and  $\mathbf{q}_b$  are the Cayley-Klein parameters.

Noting that  $U$  acts on the fundamental space  $\mathbb{C}^2$ , the irreducible representation of SU(2) at an arbitrary  $\ell$  is found by taking the  $2\ell$ -fold tensor power  $U(\mathbf{q})^{\otimes 2\ell}$  and restricting its action to the totally symmetric subspace  $\text{Sym}^{2\ell}(\mathbb{C}^2) \subset \mathbb{C}^{\otimes 2\ell}$ . This procedure is algebraically represented as,

$$D_{\text{complex}}^\ell(\mathbf{q}) = \sqrt{\frac{(\ell+m)!(\ell-m)!}{(\ell+m')!(\ell-m')!}} \sum_{\rho} (-1)^\rho \binom{\ell+m'}{\rho} \binom{\ell-m'}{\ell-\rho-m} \mathbf{q}_a^{\ell+m'-\rho} \bar{\mathbf{q}}_a^{\ell-\rho-m} \mathbf{q}_b^{\rho-m'+m} \bar{\mathbf{q}}_b^{\rho} \quad (\text{S6})$$

which defines the Wigner–D matrix.

Since we use the real-valued spherical harmonics  $Y_{\ell m}^{\text{real}}$  obtained by applying the unitary matrix  $Q$  from equation (S3), the corresponding real-valued Wigner–D matrix  $D^\ell$  used in the main text can be found by

$$D^\ell(\alpha, \beta, \gamma) = (Q^\ell)^\dagger D_{\text{complex}}^\ell Q^\ell$$

where  $^\dagger$  denotes the conjugate transpose.

### Appendix 3: Invertibility of Hessian of Spectral Overlap $\mathcal{M}$

In this section, we inspect the invertibility of the Hessians with respect to Euler angles and a unit quaternion. Note that  $\mathcal{M}$  is defined as the summation of the spectral alignment at each radial order  $n$  and angular degree  $\ell$ . Here, we fix  $n$ , because it does not depend on rotation, as well as  $\ell$  because the quadratic form in  $\mathcal{M}$  has a block-diagonal structure (consisting of  $(2\ell+1) \times (2\ell+1)$  blocks up to  $\ell_{\max}$ ) and thus the invertibility problem factorizes into each block—i.e.,  $\det[\text{diag}(A, B)] = (\det A)(\det B)$ .

#### 3.1. Lie Algebra Parameterization of Rotation

Before proceeding, we define  $\mathbf{c}_{n\ell}^{\text{evol}}$  as the column vector of azimuthal indices  $m$ ,

$$\mathbf{c}_{n\ell}^{\text{evol}} = (c_{n,\ell,-\ell}, c_{n,\ell,-\ell+1}, \dots, c_{n,\ell,\ell})^\top$$

and  $\omega_x$ ,  $\omega_y$ , and  $\omega_z$  as the parameters of the representations of Lie algebra  $\mathfrak{so}(3)$ . Finally,  $J_x^{\text{real}}$ ,  $J_y^{\text{real}}$ , and  $J_z^{\text{real}}$  refer to the representations of  $\mathfrak{so}(3)$  obtained from the change-of-basis transformation of  $J_{(\cdot)}$  via  $Q^\dagger J_{(\cdot)} Q$ . We will suppress the “real” superscript to reduce clutter in what follows.

Note that these three objects, written together as vector  $\boldsymbol{\omega} = (\omega_x, \omega_y, \omega_z)$ , are different from the Euler angles  $(\alpha, \beta, \gamma)$ . While the Euler angles describe a sequence of rotation—yaw about the body’s  $z$ -axis by  $\alpha$ , followed by pitch about the new  $y$ -axis by  $\beta$ , and finally roll about the resulting  $x$ -axis by  $\gamma$ , the components of  $\boldsymbol{\omega}$  represent the amount of rotation about the corresponding coordinate axes. Therefore, the entire rotation motion is described in one shot as,

$$\begin{aligned} D(\boldsymbol{\omega}) &= \exp(\omega_x J_x + \omega_y J_y + \omega_z J_z) \\ &= \exp(\boldsymbol{\omega} \cdot \mathbf{J}) \end{aligned} \tag{S7}$$

Differentiating with  $\boldsymbol{\omega}$  yields an expression,  $\nabla_{\boldsymbol{\omega}} D(\boldsymbol{\omega}) = D(\boldsymbol{\omega}) \cdot \mathbf{J}$ , where  $D(\boldsymbol{\omega})$  factorizes, whereas differentiating with  $\boldsymbol{\xi}$  yields (due to the fixed sequence of rotations),

$$\begin{aligned} \nabla_{\boldsymbol{\xi}} D(\boldsymbol{\xi}) &= \nabla_{\boldsymbol{\xi}} \left[ Q^\dagger (R_z^\ell(\alpha) R_y^\ell(\beta) R_x^\ell(\gamma)) Q \right] \\ &= Q^\dagger \left( \frac{\partial R_z^\ell(\alpha)}{\partial \alpha} R_y^\ell(\beta) R_x^\ell(\gamma) + \right. \\ &\quad R_z^\ell(\alpha) \frac{\partial R_y^\ell(\beta)}{\partial \beta} R_x^\ell(\gamma) + \\ &\quad \left. R_z^\ell(\alpha) R_y^\ell(\beta) \frac{\partial R_x^\ell(\gamma)}{\partial \gamma} \right) Q \end{aligned}$$

We will thus work with the Lie algebra parameters  $\boldsymbol{\omega}$  as it greatly simplifies expressions in what follows and convert back to the Euler-angle or unit-quaternion parameterizations via the Jacobian  $\nabla_{\boldsymbol{\xi}} \boldsymbol{\omega}$  and  $\nabla_{\mathbf{q}} \boldsymbol{\omega}$  at the end.

#### 3.2. Assumptions

We make the following two assumptions:

(a) The evolved shape does not have continuous rotational symmetry so its spectrum  $\mathbf{c}_{n\ell}^{\text{evol}}$  always changes under arbitrary rotations. Formally, this means that

$$(\omega_x J_x^{\text{real}} + \omega_y J_y^{\text{real}} + \omega_z J_z^{\text{real}}) \mathbf{c}_{n\ell}^{\text{evol}} = \mathbf{0} \implies \omega_x = \omega_y = \omega_z = 0.$$

(b) The Euler angles  $\boldsymbol{\xi}$  remain away from gimbal lock (e.g.,  $\beta \neq \pm\pi/2$ ) so that they provide smooth and differentiable coordinates to  $\text{SO}(3)$ .

### 3.3. Hessian of $\mathcal{M}$ with respect to Lie Algebra Parameters

Writing the spectra of both evolved and target shapes in the column vector notation, we have

$$\mathcal{M}(\boldsymbol{\omega}) = (\mathbf{c}_{n\ell}^{\text{target}})^{\top} D(\boldsymbol{\omega}) \mathbf{c}_{n\ell}^{\text{evol}}$$

The first order stationarity condition with respect to  $\boldsymbol{\omega}$  gives

$$\begin{aligned} 0 = \nabla_{\boldsymbol{\omega}} \mathcal{M}(\boldsymbol{\omega}) &= (\mathbf{c}_{n\ell}^{\text{target}})^{\top} D(\boldsymbol{\omega}) \mathbf{J} \mathbf{c}_{n\ell}^{\text{evol}} \\ &= \mathbf{u}^{\top} \mathbf{J} \mathbf{c}_{n\ell}^{\text{evol}} \end{aligned} \quad (\text{S8})$$

where we define the rotated target spectrum  $\mathbf{u} := [D(\boldsymbol{\omega})]^{\top} \mathbf{c}_{n\ell}^{\text{target}}$ .

Since the representations  $\mathbf{J}$  of the Lie algebra  $\mathfrak{so}(3)$  are skew-symmetric matrices, the condition of equation (S8) is satisfied when the evolved spectrum is parallel to  $\mathbf{u}$  (i.e.,  $\mathbf{u} = \lambda \mathbf{c}_{n\ell}^{\text{evol}}$ ).

Taking another derivative of equation (S8), we find the expression of the Hessian matrix to be,

$$\begin{aligned} \mathbf{H}_{\text{alg}} := \nabla_{\boldsymbol{\omega}}^2 \mathcal{M}(\boldsymbol{\omega}) &= (\mathbf{c}_{n\ell}^{\text{target}})^{\top} D(\boldsymbol{\omega}) (\mathbf{J} \otimes \mathbf{J}) \mathbf{c}_{n\ell}^{\text{evol}} \\ &= \lambda (\mathbf{c}_{n\ell}^{\text{evol}})^{\top} (\mathbf{J} \otimes \mathbf{J}) \mathbf{c}_{n\ell}^{\text{evol}} \end{aligned} \quad (\text{S9})$$

where we substitute in the relation for  $\mathbf{u}$  in the second line and the  $(\mathbf{J} \otimes \mathbf{J})$  denotes the outer product between the vector of the generator matrices,

$$\mathbf{J} \otimes \mathbf{J} := \begin{pmatrix} J_x \\ J_y \\ J_z \end{pmatrix} \begin{pmatrix} J_x & J_y & J_z \end{pmatrix} = \begin{pmatrix} J_x J_x & J_x J_y & J_x J_z \\ J_y J_x & J_y J_y & J_y J_z \\ J_z J_x & J_z J_y & J_z J_z \end{pmatrix}$$

Let  $\mathbf{V} = [\mathbf{v}_x, \mathbf{v}_y, \mathbf{v}_z] := [J_x \mathbf{c}_{n\ell}^{\text{evol}}, J_y \mathbf{c}_{n\ell}^{\text{evol}}, J_z \mathbf{c}_{n\ell}^{\text{evol}}] \in \mathbb{R}^{(2\ell+1) \times 3}$ . The  $ij$ -th entry of Hessian can be now written as,

$$\begin{aligned} [\mathbf{H}_{\text{alg}}]_{ij} &= \lambda \left[ (\mathbf{c}_{n\ell}^{\text{evol}})^{\top} J_i J_j \mathbf{c}_{n\ell}^{\text{evol}} \right]_{ij} \\ &= \lambda \left[ (\mathbf{c}_{n\ell}^{\text{evol}})^{\top} (-J_i^{\top}) J_j \mathbf{c}_{n\ell}^{\text{evol}} \right]_{ij} \\ &= -\lambda \left[ (J_i \mathbf{c}_{n\ell}^{\text{evol}})^{\top} (J_j \mathbf{c}_{n\ell}^{\text{evol}}) \right]_{ij} \\ &= -\lambda \mathbf{v}_i^{\top} \mathbf{v}_j \end{aligned}$$

where we use the skew-symmetry of  $J_i$  in the second equality. We recognize the Gram-matrix structure of our Hessian:  $\mathbf{H}_{\text{alg}} = -\lambda \mathbf{V}^{\top} \mathbf{V}$ .

From the assumption (a) stating the absence of rotational symmetry, we see that the three columns of  $\mathbf{V}$  are independent. Therefore, with the Singular Value Decomposition (SVD) of  $\mathbf{V}$ ,

$$\mathbf{V} = \mathbf{U} \boldsymbol{\Sigma} \mathbf{W}^{\top} \quad \text{where} \quad \boldsymbol{\Sigma} = \text{diag}(\sigma_x, \sigma_y, \sigma_z) \quad \text{with} \quad \sigma_i > 0$$

we can write the Hessian as,

$$\mathbf{H}_{\text{alg}} = -\lambda \mathbf{W} \boldsymbol{\Sigma}^2 \mathbf{W}^{\top} \quad (\text{S10})$$

where the eigenvalues are all nonzeros.

Since  $\det(\mathbf{H}_{\text{alg}}) \neq 0$ ,  $\mathbf{H}_{\text{alg}}$  is full rank and therefore invertible.

### 3.4. Converting the parameterizations

#### a. To Euler angles

To change the parameterization of rotation from the Lie algebra parameters  $\boldsymbol{\omega}$  to the Euler angles  $\boldsymbol{\xi}$ , we need  $\nabla_{\boldsymbol{\xi}} \boldsymbol{\omega}$ .

From the following closed-form relations between two parameterizations,

$$\begin{aligned}\omega_x &= \arctan2(\sin \gamma \cos \beta, \cos \gamma \cos \beta) \\ \omega_y &= \arctan2\left(-\sin \beta, \sqrt{\cos^2 \beta \cos^2 \gamma + \cos^2 \beta \sin^2 \gamma}\right) \\ \omega_z &= \arctan2(\sin \alpha \cos \beta, \cos \alpha \cos \beta)\end{aligned}$$

we obtain the Jacobian of the coordinate transformation,

$$\mathbf{J}(\alpha, \beta, \gamma) = \begin{pmatrix} 1 & 0 & -\sin \beta \\ 0 & \cos \alpha & \sin \alpha \cos \beta \\ 0 & -\sin \alpha & \cos \alpha \cos \beta \end{pmatrix} \quad \text{with} \quad \det \mathbf{J} = \cos \beta$$

which is invertible since  $\det \mathbf{J} \neq 0$  under the assumption (b).

The Euler angle Hessian  $\mathbf{H}_{\text{Euler}} = \Delta_{\xi}^{\mathbb{R}^3} \mathcal{M}$  can be obtained as,

$$\mathbf{H}_{\text{Euler}} = \mathbf{J}^T \mathbf{H}_{\text{alg}} \mathbf{J}$$

We have proven the invertibility of  $\mathbf{H}_{\text{Euler}}$  under the two assumptions since

$$\det(\mathbf{H}_{\text{Euler}}) = \det(\mathbf{J}^T \mathbf{H}_{\text{alg}} \mathbf{J}) = \det(\mathbf{J}^T) \det(\mathbf{H}_{\text{alg}}) \det(\mathbf{J}) \neq 0$$

*b. To a unit quaternion*

To make a direct connection to the proof for the Euler-angle parameterization, we work with the Lie algebra Hessian  $\mathbf{H}_{\text{alg}}$  and convert it to  $\mathbf{H}_{\text{quat}}$  via Jacobian  $\nabla_{\mathbf{q}} \boldsymbol{\omega}$ .

We begin by identifying  $\boldsymbol{\omega}$  with a pure-imaginary quaternion, i.e.,

$$(0, \omega_x, \omega_y, \omega_z) = \omega_x \mathbf{i} + \omega_y \mathbf{j} + \omega_z \mathbf{k}$$

which follows from  $\mathfrak{so}(3) \cong \text{Im}(\mathbb{H})$ . This is most easily seen by observing that their commutation relationships are identical— $[J_x, J_y] = J_z \longleftrightarrow \frac{1}{2}[\mathbf{i}, \mathbf{j}] = \mathbf{k}$ , etc. We define the magnitude  $\theta$  and the unit axis  $\hat{\mathbf{n}}$  such that:

$$\boldsymbol{\omega} = \theta \hat{\mathbf{n}} \quad \text{where } \theta = \|\boldsymbol{\omega}\| \text{ and } \|\hat{\mathbf{n}}\| = 1$$

A unit quaternion  $\mathbf{q} \in \text{SU}(2) \cong \text{SO}(3)$ , as a function of  $\boldsymbol{\omega}$ , can be obtained from the exponential map,

$$\begin{aligned}\mathbf{q}(\boldsymbol{\omega}) &= \text{Exp}\left(\frac{1}{2}\theta \hat{\mathbf{n}}\right) \\ &= \underbrace{\cos\left(\frac{\theta}{2}\right)}_{q_w} + \underbrace{\hat{\mathbf{n}} \sin\left(\frac{\theta}{2}\right)}_{(q_x, q_y, q_z) =: \mathbf{q}_v}\end{aligned}$$

where the last line is the generalization of the Euler identity,  $e^{i\theta} = \cos \theta + i \sin \theta$ , to a pure-imaginary quaternion where the 3D unit vector  $\hat{\mathbf{n}}$  takes the role of the imaginary unit  $i$ .

We invert this relationship using the logarithmic map as,

$$\begin{aligned}\boldsymbol{\omega}(\mathbf{q}_v) &= \theta \hat{\mathbf{n}} \\ &= 2 \arccos\left(\sqrt{1 - \mathbf{q}_v^\top \mathbf{q}_v}\right) \frac{\mathbf{q}_v}{\|\mathbf{q}_v\|}\end{aligned} \tag{S11}$$

where we eliminate  $q_w$  inside the arccos using the unit-norm constraint  $\|\mathbf{q}\| = 1$  to work with the 3 intrinsic independent direction parameterizing  $T_{\mathbf{q}} S^3 \subset \mathbb{R}^4$ .

Differentiating this, we find the Jacobian as,

$$\mathbf{J} = A \hat{\mathbf{q}}_v \hat{\mathbf{q}}_v^\top + B (\mathbf{I} - \hat{\mathbf{q}}_v \hat{\mathbf{q}}_v^\top)$$

where  $A = 2/\sqrt{1 - \|\mathbf{q}_v\|^2}$ ,  $B = 2 \arccos(\sqrt{1 - \|\mathbf{q}_v\|^2})/\|\mathbf{q}_v\|$ , and  $\hat{\mathbf{q}}_v = \mathbf{q}_v/\|\mathbf{q}_v\|$ .

From the rank-one perturbation structure, we immediately realize  $\hat{\mathbf{q}}_v$  is an eigenvector of  $\mathbf{J}$  with eigenvalue  $A$ ,

$$(A\hat{\mathbf{q}}_v\hat{\mathbf{q}}_v^\top + B(\mathbf{I} - \hat{\mathbf{q}}_v\hat{\mathbf{q}}_v^\top))\hat{\mathbf{q}}_v = A\hat{\mathbf{q}}_v + B(\hat{\mathbf{q}}_v - \hat{\mathbf{q}}_v) = A\hat{\mathbf{q}}_v$$

and any vector  $\mathbf{p}$  orthogonal to  $\hat{\mathbf{q}}_v$  lies in the kernel of  $\hat{\mathbf{q}}_v\hat{\mathbf{q}}_v^\top$ , and thus satisfies

$$(A\hat{\mathbf{q}}_v\hat{\mathbf{q}}_v^\top + B(\mathbf{I} - \hat{\mathbf{q}}_v\hat{\mathbf{q}}_v^\top))\mathbf{p} = B\mathbf{p}$$

so the remaining two eigenvectors both have eigenvalue  $B$ . The determinant of  $\mathbf{J}$  is therefore,

$$\det \mathbf{J} = AB^2 = \frac{8 \arccos^2(\sqrt{1 - \|\mathbf{q}_v\|^2})}{\|\mathbf{q}_v\|^2 \sqrt{1 - \|\mathbf{q}_v\|^2}}$$

which is finite for every unit quaternion except at  $\|\mathbf{q}_v\|=1$  (i.e.,  $q_w=0$ ), which corresponds to  $180^\circ$  rotation. Therefore,  $\mathbf{H}_{\text{quat}} = \mathbf{J}^\top \mathbf{H}_{\text{alg}} \mathbf{J}$  is invertible everywhere except at this configuration. Note that this point singularity is unlikely to be reached exactly during numerical computation, whereas gimbal lock is a 2-dimensional region of  $\text{SO}(3)$ .

Importantly, this point singularity does not originate from the quaternion itself. Instead, it is introduced by the procedure of converting a unit quaternion  $\mathbf{q} \in \text{SU}(2)$  to the Lie algebra parameter  $\boldsymbol{\omega} \in \mathfrak{su}(2)$  via the logarithmic map of equation (S11), which is ill-defined when  $q_w=0$ . By contrast, the parameterization used in equation (S6) never invokes the logarithm and depends only on polynomial combinations of the quaternion components. Thus, the point singularity at  $180^\circ$  rotation is not a property of the unit quaternion parameterization itself, nor of the Wigner–D construction; it is solely an artifact of forcing a globally nonlinear  $\text{SU}(2)$  manifold into a single 3-dimensional coordinate chart of the Lie algebra.

### 3.5. Realization of Assumptions During Training

The assumption (a) is automatically realized due to the discrete nature of the point cloud—the positions of the agents can never be perfectly arranged in a way that the resulting Zernike spectrum remains unchanged under arbitrary infinitesimal rotations. However, a point cloud may produce small rotational eigenvalues. To improve conditioning, we slightly elongate the initial positions of agents and add noise at the beginning of each iteration, as detailed in ‘Preparation of initial states’ section in the Methods of the main text. As a safeguard against potentially small eigenvalues, we compute the  $\mathbf{H}_{\text{quat}}$  using the Moore–Penrose pseudoinverse with a threshold of 0.01, which automatically removes the null radial component in the  $4 \times 4$  Hessian.

### Appendix 4: Riemannian Hessian from Euclidean Hessian

The variation of  $\nabla_{\mathbf{q}}^{S^3} \mathcal{M}$  of equation (9) of the main text under  $\mathbf{q} \mapsto \mathbf{q} + \delta\mathbf{q}$ ,

$$\delta \left[ \nabla_{\mathbf{q}}^{S^3} \mathcal{M} \right] = -(\delta\mathbf{q}\mathbf{q}^\top + \mathbf{q}\delta\mathbf{q}^\top) \nabla_{\mathbf{q}} \mathcal{M} + (\mathbf{I} - \mathbf{q}\mathbf{q}^\top) \nabla_{\mathbf{q}\mathbf{q}}^2 \mathcal{M} \delta\mathbf{q} \quad (\text{S12})$$

Once we project it on to the tangent space using  $\mathbf{P} = (\mathbf{I} - \mathbf{q}\mathbf{q}^\top)$ ,

$$\begin{aligned} \mathbf{P} \delta \left[ \nabla_{\mathbf{q}}^{S^3} \mathcal{M} \right] &= -\mathbf{P} \delta\mathbf{q} \mathbf{q}^\top \nabla_{\mathbf{q}} \mathcal{M} + \mathbf{P} \mathbf{q} \delta\mathbf{q}^\top \nabla_{\mathbf{q}} \mathcal{M} + \mathbf{P}^2 \nabla_{\mathbf{q}\mathbf{q}}^2 \mathcal{M} \delta\mathbf{q} \\ &= -\delta\mathbf{q} \mathbf{q}^\top \nabla_{\mathbf{q}} \mathcal{M} + \mathbf{P} \nabla_{\mathbf{q}\mathbf{q}}^2 \mathcal{M} \delta\mathbf{q} \\ &= [\mathbf{P} \nabla_{\mathbf{q}\mathbf{q}}^2 \mathcal{M} - \alpha \mathbf{I}] \delta\mathbf{q} \end{aligned}$$

where we use  $\mathbf{q}^\top \delta\mathbf{q} = 0$  in the first term because  $\mathbf{q} \perp \delta\mathbf{q}$  and define  $\alpha = \mathbf{q}^\top \nabla_{\mathbf{q}} \mathcal{M}$ .

The above expression is derived as a directional derivative along  $\delta\mathbf{q} \in T_{\mathbf{q}} S^3$ . To obtain the generic operator expression of the Riemannian Hessian,  $\text{Hess}_{S^3} \mathcal{M} : T_{\mathbf{q}} S^3 \rightarrow T_{\mathbf{q}} S^3$ , we multiply with  $\mathbf{P}$  from the right to restrict the domain to the tangent space,

$$\text{Hess}_{S^3} \mathcal{M} = \mathbf{P} (\nabla_{\mathbf{q}\mathbf{q}}^2 \mathcal{M} - \alpha \mathbf{I}) \mathbf{P}$$

which recovers the expression of equation (11) of the main text.

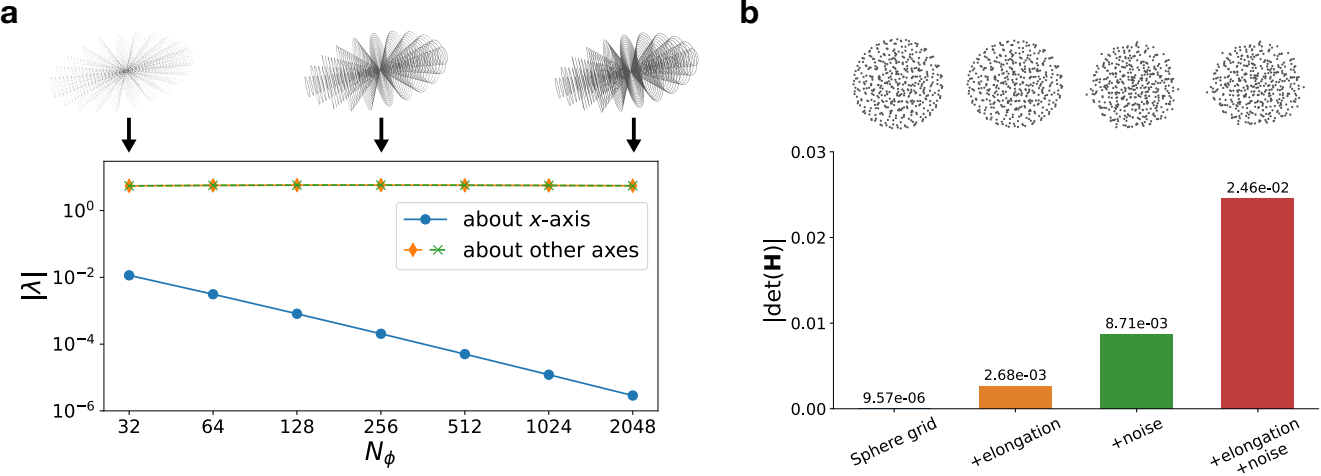


FIG. S1. Numerical verification of rotational symmetry. (a) Magnitudes of the eigenvalues of rotational Hessian  $\mathbf{H}_q$  of ellipsoid-shaped point clouds with varying number of azimuthal partitions  $N_\phi$  around the symmetry (elongation) axis. One eigenvalue is several orders of magnitude smaller than the other two, reflecting the axisymmetric nature of the ellipsoid. As  $N_\phi$  increases, the  $N_\phi$ -fold cyclic symmetry approaches continuous symmetry, and the eigenvalue along the symmetry axis decreases in line with this trend. (b) Determinant of  $\mathbf{H}_q$  of sphere-shaped point clouds under different perturbations. The unperturbed sphere grid yields a small but nonzero determinant due to its discrete nature and small nonuniformity induced by the Poisson-disk sampling. Adding noise increases the determinant more than elongation does, since the elongated shape remains symmetric about one axis. Combining elongation and noise produces a shape with a determinant nearly five orders of magnitude larger, which is used in the experiments shown in the main text.

#### Appendix 5: Rotational symmetry in practice

The rotational symmetry of shapes discussed in the Hessian invertibility proof in Section 3 is a continuous symmetry. Since the morphogenesis simulation operates on a discrete point cloud, it is not immediately clear to what extent the Hessian is sensitive to the symmetry represented by discrete points. To examine this, we study how the magnitudes of the Hessian's eigenvalues scale with the number of azimuthal partitions  $N_\phi$  around the symmetry axis of an ellipsoid (Fig. S1a). We evaluate the spectral overlap  $\mathcal{M}$  (equation (8) of the main text) using  $\mathbf{C}^{\text{eval}} = \mathbf{C}^{\text{target}}$ , obtained from an  $x$ -axis aligned ellipsoid, and compute its gradient with respect to a unit quaternion that rotates the ellipsoid by  $+1^\circ$  about the  $x$ -axis. This quaternion  $\mathbf{q}_x$  is constructed by converting the axis-angle coordinate  $(\mathbf{n}, \theta)$  with  $\mathbf{n}$  coincides with the  $x$ -axis. The resulting Hessian in  $\mathbb{R}^4 \times \mathbb{R}^4$  is converted into the tangent space Hessian in  $T_{\mathbf{q}_x} S^3 \times T_{\mathbf{q}_x} S^3$  using an orthonormal frame  $\mathbf{U} \in \mathbb{R}^{4 \times 3}$ . We obtain this frame via QR decomposition of the matrix whose first column is  $\mathbf{q}_x$  and the remaining columns are chosen from basis vectors in  $\mathbb{R}^4$ . Any potential sign flips in the resulting frame do not affect our analysis, as we compare only the absolute magnitudes of the eigenvalues. We find that the rotational symmetry is already evident in the discrete point cloud at resolutions as low as  $N_\phi = 32$ , as indicated by several orders of magnitude of separation in one of the tangent-space eigenvalues. As  $N_\phi$  increases and the ellipsoidal point cloud forms smooth rings, one rotational eigenvalue becomes negligibly small, reflecting the discrete  $N_\phi$ -fold cyclic symmetry of the point cloud approaching the true continuous rotational symmetry.

We next examine the behavior of the Hessian determinant in the actual experimental setting of DiffeoMorph, using the shell+core sphere grid described in ‘Preparation of initial states’ section in the Methods of the main text and adding relevant perturbations on it (Fig. S1b). We compute the spectral overlap  $\mathcal{M}$  using the Zernike moments  $\mathbf{C}^{\text{sph}}$  of the sphere-derived point clouds as both input and target—i.e.,  $\mathcal{M}(\mathbf{C}^{\text{sph}}, \mathbf{C}^{\text{sph}})$ —and evaluate the Hessians at the unit quaternion corresponding to  $+1^\circ$  rotation about the  $x$ -axis. We verify that the results do not depend on the specific choice of unit quaternion. This observation is consistent with the mathematical structure of  $\mathbf{H}_{\text{quat}}$  described in Section 3, where its determinant is determined by the rotational eigenvalues of the Lie algebra Hessian  $\mathbf{H}_{\text{alg}}$  in equation S10. Because a sphere is symmetric about any axis, the original sphere-shaped point cloud yields a very small Hessian determinant. Elongating the sphere breaks this symmetry and reduces the number of small eigenvalues to one, and the determinant value increases accordingly. Separately, adding zero-mean Gaussian noise with magnitude 0.05 perturbs the grid enough to distort the spherical appearance, leading all three rotational eigenvalues to increase. In DiffeoMorph experiments, these two perturbations are applied jointly: elongation serves as morphogen-mediated symmetry breaking, while noise encourages generalizable learning. The resulting point cloud has a substantially

larger determinant than the original sphere grid. This indicates that the gradient of the inner alignment step can be computed robustly via implicit differentiation, which requires inverting the Hessian.

## Appendix 6: Advantages of unit quaternion over Euler angles

### 6.1. Gradient-based optimization on $\text{SO3}$

As emphasized in assumption (b) of the invertibility proof in Section 3, Euler angle parameterizations of rotation suffers from gimbal lock, which occurs when two of the three rotation axes become aligned, resulting in a loss of one degree of freedom and a degeneracy in the mapping from Euler angles to physical rotations. In the proof, this degeneracy manifests as a singularity in the Jacobian of the coordinate transformation to Lie algebra parameters. Fig. S2 illustrates that gimbal lock affects the shape-matching loss even earlier in the computation: the alignment optimization can prematurely stall as soon as the optimization path reaches a gimbal lock configuration. In this experiment, the task is to align the spectrum of the bunny shown on the left to that of the bunny on the right by maximizing the spectral overlap  $\mathcal{M}$ . We compare efficiency of gradient-based optimizations using Euler angles versus a unit quaternion. The Euler-angle trajectory stalls due to vanishing gradients near the north pole—corresponding to the gimbal-lock condition  $\beta=0^\circ$ —consequently fails to align the two shapes. In contrast, the unit quaternion parameterization avoids this singularity entirely, allowing optimization to proceed smoothly and achieve the correct alignment with maximal spectral overlap.

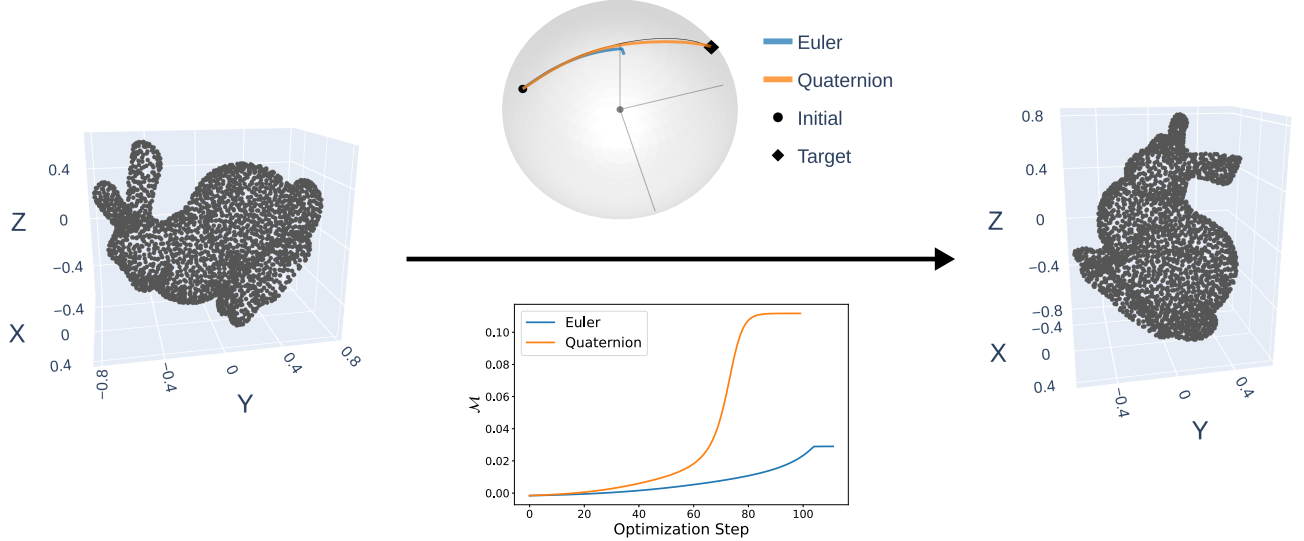


FIG. S2. Comparison of gradient-based optimization on  $\text{SO}(3)$  using Euler angles and unit quaternion parameterizations. The goal is to align the spectrum of the bunny rotated by  $+45^\circ$  about the x-axis (left) to that of the bunny rotated by  $-45^\circ$  (right). To visualize the optimization of the two parameterizations both of which have three degrees of freedom on a sphere, we only show the unit rotation axis  $\mathbf{n}$  of the axis-angle coordinates  $(\mathbf{n}, \theta)$  where  $\theta$  is the rotation angle about  $\mathbf{n}$  (top center). Note that the alignment can be achieved simply by rotating  $\mathbf{n}$  while keeping  $\theta=0^\circ$  throughout. The optimization trajectories of both parameterizations progress smoothly towards the north pole, which is a gimbal lock for Euler angles. At this region, the Euler angle trajectory stalls due to vanishing gradients, whereas the unit quaternion trajectory passes through and reaches the target. Learning curves of the spectral overlap  $\mathcal{M}$  highlight the premature convergence of the alignment optimization when using Euler angles compared to using unit quaternion (bottom center).

### 6.2. Hessian of spectral overlap $\mathcal{M}$

Next, we inspect the behavior of the rotational Hessian along the Spherical Linear Interpolation (SLERP) [77] path between the two bunnies (Fig. S3a). We compute the spectral overlap  $\mathcal{M}$  using the Zernike moments of the left bunny  $\mathbf{C}^{\text{left}}$  and its rotated spectrum as the target  $\mathbf{C}^{\text{target}} = D(\cdot) \mathbf{C}^{\text{left}}$  where the Wigner-D matrix is evaluated either from a unit quaternion or Euler angles along the SLERP path. We apply the same rotation to  $\mathbf{C}^{\text{left}}$  and evaluate the Hessian

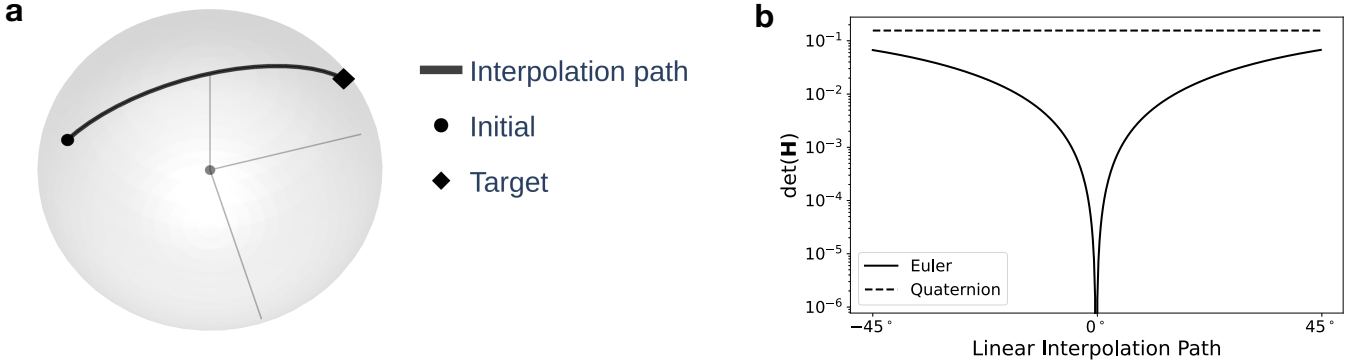


FIG. S3. Comparison of Hessians for Euler angles and unit quaternion parameterizations. (a) Since Fig. S2 above illustrates only gradient behavior—without the Hessian inversion relevant to shape learning of DiffeoMorph, the inverse Hessians of the two parameterizations are evaluated here along the linear interpolation path between the two bunny orientations. (b) At the gimbal lock configuration (north pole), the determinant of Hessian for the Euler angle parameterization approaches zero due to having singularity at this point. Note that this behavior differs from that in Fig. S1, where small determinants arise from small eigenvalues associated with rotational symmetry. In contrast, the unit quaternion provides a smooth global parameterization and thus avoids this pathology.

with respect to the corresponding parameters. As shown in Fig. S3b, the Hessian determinant under the Euler angle parameterization collapses to zero at the  $0^\circ$  point along the SLERP path, which corresponds to the north-pole gimbal lock where the Jacobian becomes rank-deficient. In contrast, singularity-free quaternion parameterization allows its Hessian determinant to remain finite over the entire path.

#### Appendix 7: Extension to Zernike moments to higher-order tensor

We can generalize the weight associated to each point from a scalar to any type- $(p, q)$  tensor. Since these objects transform under rotation, the spatial (i.e., Cartesian) index of the corresponding Zernike moments should also be transformed away via the spatial rotation matrix  $R$ . For example, the  $\ell$ -th order Zernike moments  $\mathbf{z}_\ell$  obtained from vector-valued weights have the azimuthal index  $m$  and a spatial index  $i \in \{x, y, z\}$ . Each of them can be rotated with the spectral rotation matrix  $D$  and the spatial rotation matrix  $R$ , respectively, as follows,

$$z_{\ell m i} = \sum_{m'=-\ell}^{\ell} \sum_{j=1}^3 D_{mm'}^\ell(\xi) R_{ij}(\xi) z_{\ell m' j}$$

For the higher-order tensor with both upper (contravariant) and lower (covariant) indices, we can use  $R$ —as  $(1, 1)$  tensor—and  $R^{-1} = R^\top$  to transform the respective indices. This formulation enables learning general tensor-valued quantities associated with agents, such as their velocity or stress tensor. Extending the method to compare such internal states at intermediate times, thereby imposing more realistic constraints on morphogenesis dynamics, is a promising direction for future work.

#### Appendix 8: Details of SDE integration

The pseudocode of the computation procedure in our  $\text{SE}(3)$ -equivariant force model is shown in Algorithm S1.

---

**Algorithm S1** Force computation in the SE(3)-Equivariant Morphogenesis Model
 

---

**Input:** Initial positions  $X = \{x_i\}$ , gene states  $G = \{g_i\}$ , polarity vectors  $P = \{p_i\}$

**Learned model components:**

$\phi_\ell$ : equilibrium length MLP  
 $\phi_e$ : edge message MLP  
 $\phi_\alpha$ : attention MLP  
 $\phi_x$ : force-scaling MLP  
 $\phi_g$ : gene update MLP  
 $\phi_p$ : polarity update MLP

**Initialize:**  $t \leftarrow 0$

**while**  $t < T$  **do**

**for** all pairs of agents  $(i, j)$  **do**

    Compute distance:  $d_{ij} \leftarrow \|x_i - x_j\|$   
     Compute angle:  $\theta_{ij} \leftarrow \arccos(p_i \cdot p_j)$   
     Predict equilibrium length:  $\ell_{ij} \leftarrow \phi_\ell(g_i, g_j)$   
     Construct edge feature:  $e_{ij} \leftarrow [g_i \| g_j \| d_{ij} \| \theta_{ij}]$   
     Compute message:  $m_{ij} \leftarrow \phi_e(e_{ij})$   
     Compute attention:  $\alpha_{ij} \leftarrow \text{softmax}_j[\phi_\alpha(e_{ij})]$

**end for**

**for** all agents  $i$  **do**

    Aggregate message:  $m_i \leftarrow \sum_{j \neq i} \alpha_{ij} m_{ij}$   
     Update gene state:  $\dot{g}_i \leftarrow \phi_g([g_i \| m_i])$   
     Update polarity:  $\dot{p}_i \leftarrow \phi_p([g_i \| m_i])$   
     Compute force:

$$\dot{x}_i \leftarrow \sum_{j \neq i} \alpha_{ij} \left( 1 - \frac{\ell_{ij}}{d_{ij}} \right) (x_i - x_j) \cdot \phi_x(m_{ij})$$

**end for**

  Integrate position:  $x_i \leftarrow x_i + \dot{x}_i \cdot \Delta t$

  Integrate gene state:  $g_i \leftarrow g_i + \dot{g}_i \cdot \Delta t$

  Integrate polarity (renormalized):  $p_i \leftarrow \text{normalize}(p_i + \dot{p}_i \cdot \Delta t)$

$t \leftarrow t + \Delta t$

**end while**

---

#### Appendix 9: Runtime analysis for direct vs. implicit gradient

To quantify the time saved by implicit differentiation, we perform the direct shape optimization experiment from Fig. 2d with  $N = 1000$  point cloud using standard direct backpropagation and implicit differentiation. We measure the runtime of a single outer training step—which involves a forward step (including alignment steps), a backward pass (either via direct or implicit), and a gradient update—as a function of the number of alignment steps taken for optimizing unit quaternion. After compiling the training function, we execute it on the GPU five times and report the mean values in Fig. S4. We omit showing error bar because the runtime fluctuation is minimal. In both methods, runtime increases with the number of alignment steps since these iterations correspond directly to the forward computations within the loss. However, direct backpropagation must unroll all forward iterations during the backward pass, whereas implicit differentiation computes the gradient  $\nabla_{\mathbf{X}} \mathbf{q}^*$  in a single step. This yields a substantial runtime advantage, as reflected in the flatter slope for the implicit method. In DiffeoMorph experiments using learning rate  $\eta_{\text{inner}} = 1\text{e-}2$  and convergence threshold  $\delta_{\text{inner}} = 1\text{e-}7$ , the unit quaternion optimization typically converges in approximately 300 iterations. Therefore, employing implicit differentiation provides roughly a fivefold reduction in training time.

#### Appendix 10: Model benchmarking

We benchmark our force model against graph-based Neural Cellular Automata (NCA), which support continuous-space agent motion. For a fair comparison, we adopt their architectures as the force model of numerical integration and train them using our shape-matching loss. Specifically, we use GNCA [22], which employs the GeneralConv layer of You *et al.* [78], and its equivariant extension E(n)-GNCA [33]. Both models are trained using the same noise levels as in our experiments (0.05 $\epsilon$  for ellipsoid and crescent, and 0.03 $\epsilon$  for bunny). Tab. S1 reports the means and standard deviations of the shape-matching loss: the Nois columns summarize performance over 10 noise realizations, while the

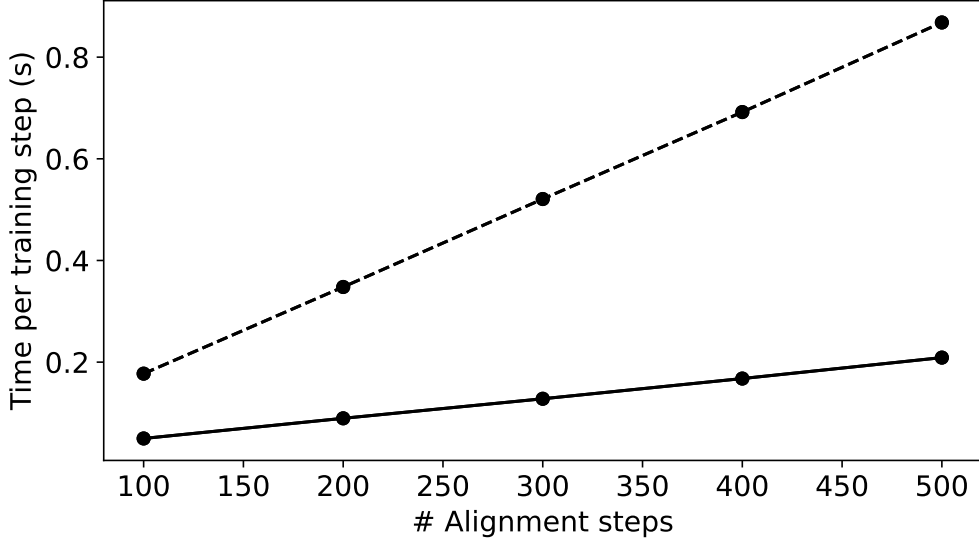


FIG. S4. Average runtime per direct  $\mathbf{X}$  optimization step ( $n=5$ ) as a function of the number of inner optimization steps in spectral alignment. The runtime under standard backpropagation (“direct,” dashed line) increases at a rate of 1.7ms per step, whereas implicit differentiation (“Implicit,” solid line) grows more slowly, at 0.4 ms per step.

Shift columns average over the additional 10 random orientations per noise—identical protocol as in Fig. 4. GNCA attains high loss because it fails to train. Unlike the paper’s training setting—where informative initial features (e.g, normalized target positions or fixed random features) are provided—DiffeoMorph requires the model to guide agents purely from their internal states with minimal spatial cues, making the learning task substantially more difficult. In contrast, E( $n$ )-GNCA (which corresponds to our model without attention, equilibrium length, and polarity) trains successfully and achieves far better generalization. With enhanced neighbor sensing mechanisms and directional features, our full model achieves the strongest performance across all conditions.

|                               |                 | Ellipsoid       |                  | Crescent         |                  | Bunny           |                  |
|-------------------------------|-----------------|-----------------|------------------|------------------|------------------|-----------------|------------------|
|                               |                 | Noise           | Shift            | Noise            | Shift            | Noise           | Shift            |
| <b>GNCA</b>                   | No noise        | 26.16           | $27.14 \pm 0.56$ | 23.04            | $24.19 \pm 0.86$ | 12.15           | $12.66 \pm 0.27$ |
| <b>E(<math>n</math>)-GNCA</b> | No noise        | 1.18            | $1.47 \pm 0.07$  | 2.69             | $2.83 \pm 0.12$  | 0.84            | $1.34 \pm 0.11$  |
|                               | $+0.05\epsilon$ | $1.16 \pm 0.12$ | $1.92 \pm 0.17$  | $3.78 \pm 0.26$  | $3.89 \pm 0.42$  | $1.27 \pm 0.09$ | $1.84 \pm 0.18$  |
|                               | $+0.1\epsilon$  | $3.08 \pm 0.47$ | $3.31 \pm 0.31$  | $8.56 \pm 0.67$  | $9.49 \pm 0.99$  | $2.42 \pm 0.15$ | $3.42 \pm 0.14$  |
|                               | $+0.2\epsilon$  | $6.39 \pm 0.68$ | $5.79 \pm 0.71$  | $15.36 \pm 0.86$ | $15.62 \pm 1.04$ | $5.60 \pm 0.49$ | $6.09 \pm 0.53$  |
| <b>DiffeoMorph (ours)</b>     | No noise        | 0.73            | $0.89 \pm 0.12$  | 1.14             | $1.23 \pm 0.11$  | 0.24            | $0.36 \pm 0.05$  |
|                               | $+0.05\epsilon$ | $1.15 \pm 0.08$ | $1.21 \pm 0.16$  | $1.89 \pm 0.12$  | $1.97 \pm 0.20$  | $0.42 \pm 0.03$ | $0.60 \pm 0.09$  |
|                               | $+0.1\epsilon$  | $2.79 \pm 0.28$ | $3.36 \pm 0.62$  | $3.89 \pm 0.28$  | $4.66 \pm 0.56$  | $0.87 \pm 0.11$ | $1.11 \pm 0.17$  |
|                               | $+0.2\epsilon$  | $5.89 \pm 1.02$ | $5.04 \pm 0.9$   | $8.49 \pm 1.14$  | $9.96 \pm 1.51$  | $2.34 \pm 0.30$ | $2.45 \pm 0.42$  |

TABLE S1. Benchmarking against Graph Neural Cellular Automata (GNCA) models. The Vanilla GNCA model fails to train, resulting in poor test performances. Its equivariant extension, E( $n$ )-GNCA successfully learns to reproduce target shapes and achieves loss values an order of magnitude smaller. Our model further improves upon E( $n$ )-GNCA, achieving consistently lower errors across all shapes and conditions.

#### Appendix 11: Mathematical expressions of benchmark distance metrics

We summarize here the mathematical expressions of the distance metrics compared in ‘Benchmarking shape-matching objective’ section in the Results of the main text for the readers’ convenience. Let  $N$  and  $M$  denote the number of points in coordinate matrices  $\mathbf{X}$  and  $\mathbf{Y}$  respectively, and  $|\cdot|$  denotes cardinality of a set.

$$\begin{aligned}
\text{Chamfer} : & \quad \frac{1}{N} \sum_{i=1}^N \min_j \|\mathbf{x}_i - \mathbf{y}_j\|^2 + \frac{1}{M} \sum_{j=1}^M \min_i \|\mathbf{y}_j - \mathbf{x}_i\|^2 \\
\text{Earth Mover's} : & \quad \min_{\pi \in \Pi(\mathbf{a}, \mathbf{b})} \sum_{i=1}^N \sum_{j=1}^M \pi_{ij} \|\mathbf{x}_i - \mathbf{y}_j\| \\
\text{Pairwise} : & \quad \frac{1}{N^2} \sum_{i,j=1}^N (\|\mathbf{x}_i - \mathbf{x}_j\| - \|\mathbf{y}_i - \mathbf{y}_j\|)^2 \\
\text{Gromov-Wasserstein} : & \quad \min_{\pi \in \Pi(\mathbf{a}, \mathbf{b})} \sum_{i,i'=1}^N \sum_{j,j'=1}^M \pi_{ij} \pi_{i'j'} (\|\mathbf{x}_i - \mathbf{x}_{i'}\| - \|\mathbf{y}_j - \mathbf{y}_{j'}\|)^2 \\
\text{Power Spectrum} : & \quad \frac{1}{n_{\max} \ell_{\max}} \sum_n^{n_{\max}} \sum_{\ell}^{\ell_{\max}} (\mathbf{A}_{n\ell}^{\mathbf{X}} - \mathbf{A}_{n\ell}^{\mathbf{Y}})^2 \\
\text{Bispectrum} : & \quad \frac{1}{n_{\max} |\mathcal{I}_{\mathcal{B}}|} \sum_n^{n_{\max}} \sum_{(\ell_1, \ell_2, \ell_3) \in \mathcal{I}_{\mathcal{B}}} (\mathbf{B}_{n\ell_1 \ell_2 \ell_3}^{\mathbf{X}} - \mathbf{B}_{n\ell_1 \ell_2 \ell_3}^{\mathbf{Y}})^2 \\
\text{Trispectrum} : & \quad \frac{1}{n_{\max} |\mathcal{I}_{\mathcal{T}}|} \sum_n^{n_{\max}} \sum_{(\ell_1, \ell_2, \ell_3, \ell_4) \in \mathcal{I}_{\mathcal{T}}} (\mathbf{T}_{n\ell_1 \ell_2 \ell_3 \ell_4}^{\mathbf{X}} - \mathbf{T}_{n\ell_1 \ell_2 \ell_3 \ell_4}^{\mathbf{Y}})^2
\end{aligned}$$

In the Earth Mover's and Gromov-Wasserstein distances,  $\Pi(\mathbf{a}, \mathbf{b})$  denotes the set of all discrete transport plans (i.e., probabilistic coupling matrices) between two discrete mass vectors  $\mathbf{a} = (\frac{1}{N}, \dots, \frac{1}{N})^\top$  and  $\mathbf{b} = (\frac{1}{M}, \dots, \frac{1}{M})^\top$ .  $\mathcal{I}_{\mathcal{B}}$  of Bispectrum refers to the set of all triplet  $(\ell_1, \ell_2, \ell_3)$  of angular degree combinations that satisfy the selection rules:

$$\text{Angular momentum coupling} : |\ell_1 - \ell_2| \leq \ell_3 \leq \ell_1 + \ell_2$$

$$\text{Parity constraint} : \ell_1 + \ell_2 + \ell_3 = \text{Even Integer}$$

Similarly,  $\mathcal{I}_{\mathcal{T}}$  is the set of all quartet  $(\ell_1, \ell_2, \ell_3, \ell_4)$ , together with  $\ell' \in \mathcal{L}(\ell_1, \ell_2, \ell_3, \ell_4)$ , that satisfy the selection rules:

$$\text{Angular momentum coupling} : |\ell_1 - \ell_2| \leq \ell' \leq \ell_1 + \ell_2 \quad \text{and} \quad |\ell_3 - \ell_4| \leq \ell' \leq \ell_3 + \ell_4$$

$$\text{Parity constraint} : \ell_1 + \ell_2 + \ell' = \ell_3 + \ell_4 + \ell' = \text{Even Integer}$$

The two-, three- and four-point invariants  $\mathbf{A}_{n\ell}^{(\cdot)}$ ,  $\mathbf{B}_{n\ell_1 \ell_2 \ell_3}^{(\cdot)}$ , and  $\mathbf{T}_{n\ell_1 \ell_2 \ell_3 \ell_4}^{(\cdot)}$  in Power spectrum, Bispectrum, and Trispectrum are:

$$\begin{aligned}
\mathbf{A}_{n\ell} &= \frac{1}{2\ell + 1} \sum_{m=-\ell}^{\ell} (c_{n\ell m}^{(\cdot)})^2 \\
\mathbf{B}_{n\ell_1 \ell_2 \ell_3}^{(\cdot)} &= \sum_{m_1=-\ell_1}^{\ell_1} \sum_{m_2=-\ell_2}^{\ell_2} \sum_{m_3=-\ell_3}^{\ell_3} C_{\ell_1 m_1 \ell_2 m_2}^{\ell_3 m_3} \tilde{c}_{n\ell_1 m_1}^{(\cdot)} \tilde{c}_{n\ell_2 m_2}^{(\cdot)} \tilde{c}_{n\ell_3 m_3}^{(\cdot)} \\
\mathbf{T}_{n\ell_1 \ell_2 \ell_3 \ell_4}^{(\cdot)} &= \sum_{\ell' \in \mathcal{L}(\ell_1, \ell_2, \ell_3, \ell_4)} \sum_{m_1=-\ell_1}^{\ell_1} \sum_{m_2=-\ell_2}^{\ell_2} \sum_{m_3=-\ell_3}^{\ell_3} \sum_{m_4=-\ell_4}^{\ell_4} \sum_{m'=-\ell'}^{\ell'} C_{\ell_1 m_1 \ell_2 m_2}^{\ell' m'} C_{\ell_3 m_3 \ell_4 m_4}^{\ell' m'} \tilde{c}_{n\ell_1 m_1}^{(\cdot)} \tilde{c}_{n\ell_2 m_2}^{(\cdot)} \tilde{c}_{n\ell_3 m_3}^{(\cdot)} \tilde{c}_{n\ell_4 m_4}^{(\cdot)}
\end{aligned}$$

where  $C_{\ell_1 m_1 \ell_2 m_2}^{\ell_3 m_3}$  is the Clebsch-Gordan coefficient tensor that couples the three angular momentum components,  $\tilde{c}_{n\ell m}^{(\cdot)} = c_{n\ell m}^{(\cdot)} / \sqrt{\bar{c}_{\ell}^{(\cdot)}}$  and  $\bar{c}_{\ell}^{(\cdot)} = \frac{1}{n_{\max} (2\ell + 1)} \sum_n^{n_{\max}} \sum_{m=-\ell}^{\ell} (c_{n\ell m}^{(\cdot)})^2$ .

Note that  $\mathbf{A}$ ,  $\mathbf{B}$ , and  $\mathbf{T}$  can be interpreted as the Fourier domain equivalents of the two-, three, and four-point correlation functions in the spatial domain,  $C_2(\mathbf{r}_1, \mathbf{r}_2)$ ,  $C_3(\mathbf{r}_1, \mathbf{r}_2, \mathbf{r}_3)$ , and  $C_4(\mathbf{r}_1, \mathbf{r}_2, \mathbf{r}_3, \mathbf{r}_4)$ .